Ultrasound Elastography: Time Delay Estimation

Hoda Sadat Hashemi

A Thesis

in

The Department

of

Electrical and Computer Engineering

Presented in Partial Fulfillment of the Requirements

for the Degree of

Master of Applied Science (Electrical Engineering) at

Concordia University

Montréal, Québec, Canada

July 2017

CONCORDIA UNIVERSITY

School of Graduate Studies

This is to certify that the thesis prepared

By: **Hoda Sadat Hashemi**

Entitled: **Ultrasound Elastography: Time Delay Estimation**

and submitted in partial fulfillment of the requirements for the degree of

Master of Applied Science (Electrical Engineering)

complies with the regulations of this University and meets the accepted standards with respect to originality and quality.

Signed by the Final Examining Committee:

_____ Chair
Dr. R. Raut

_____ External Examiner
Dr. N. Bouguila

_____ Examiner
Dr. M. O. Ahmad

_____ Supervisor
Dr. H. Rivaz

Approved by _____
Dr. W. E. Lynch, Chair
Department of Electrical and Computer Engineering

_____ 2017

_____
Dr. A. Asif, Dean
Faculty of Engineering and Computer Science

Abstract

Ultrasound Elastography: Time Delay Estimation

Hoda Sadat Hashemi

A critical step in quasi-static ultrasound elastography is estimation of time-delay between two frames of Radio-Frequency (RF) data that are obtained while tissue is undergoing deformation. This thesis presents a novel technique for Time-Delay Estimation (TDE) of *all samples of RF data simultaneously*. A nonlinear cost function that incorporates similarity of RF data intensity and prior information of displacement continuity is formulated. Optimization of this nonlinear function involves searching for TDE of all samples of RF data, rendering the optimization intractable with conventional techniques given that the number of variables can be approximately one million. Therefore, the optimization problem is converted to a sparse linear system of equations, and is solved in real-time using a computationally efficient optimization technique. We call our method GLUE (GLobal Ultrasound Elastography), and compare it to Dynamic Programming Analytic Minimization (DPAM) (Rivaz, Boctor, Choti, & Hager, 2011) and Normalized Cross Correlation (NCC) techniques. We test our method on simulation, phantom, and *in-vivo* data. The results show that the proposed method outperforms both DPAM and NCC techniques. In another proposed method, we assume tissue deformation can be efficiently approximated by an affine transformation, and hence call our method ATME (Affine Transformation Model Elastography). The affine transformation model is utilized to obtain initial estimates of axial and lateral displacement fields. The nonlinear cost function of GLUE method is used to fine-tune the initial affine deformation field. Results on simulation and RF data we collect from *in-vivo* patellar tendon and medial collateral ligament (MCL), show that ATME can be used to accurately track tissue displacement.

Acknowledgments

My appreciation, first goes to my knowledgeable, innovative and genius supervisor, Prof. Hassan Rivaz, for his awesome supervision which brought me a wonderful academic life at Concordia University. His dedication and full support above all his awesome guidance and novel ideas have helped me to accomplish this work. His energetic personality consistently motivated me to push forward my research. I would never forget his affection and warmth throughout my research period, and I am deeply grateful for them.

I would like to thank my colleagues and friends in the research group of my professor, IMPACT group, for their great discussions. Also, I do appreciate Dr. Mathieu Boily and Dr. Paul A. Martineau from McGill University, and also Dr. Robert Kilgour from Concordia exercise science department for their invaluable discussions and collaborations in my work.

I would like to acknowledge the financial support from the Richard and Edith Strauss Canada Foundation throughout my graduate work at Concordia University.

Finally, I would like to express my gratitude to my parents and sisters for their love and lasting supports. I would like to thank my grandmother for her continuous encouragements and fervent hope.

Contents

List of Figures

List of Tables

Chapter 1

Introduction

This chapter provides a brief summary on some ultrasound imaging principles. We then focus on ultrasound elastography which is the main concentration of this thesis.

1.1 Ultrasound Imaging

Medical imaging has brought great advances in disease diagnostic and treatment during recent decades. Ultrasound is sound waves which have higher frequencies than the range of human hearing (20 Hz-20kHz). It has meanwhile emerged as an attractive medical imaging approach due to its numerous advantages. Anatomy, tissue characterization, and dynamic movement of organs can be investigated using ultrasound. Furthermore, it is safe, easy to use, portable and cost efficient.

In Figure 1.1, an Alpinion E-CUBE 12R ultrasound system is shown. One of the important parts of the ultrasound imaging system is the transducer probe which consists of piezoelectric material or crystals. Applying electrical voltage to these crystals produces acoustic signals that travel outward. The waves propagate into the body and hit the boundary between different tissues. Some reflections of acoustic waves back scatter to the probe, whereas, the rest penetrate deeper into the tissue and reflect after hitting another boundary. The transducer receives the reflected waves and sends them back to the machine as the electrical currents. By using the speed of sound and arrival time of each reflection to the probe, the distance between the probe and tissue is calculated. The intensities and distances of the echoes are shown on the screen as an ultrasound image as illustrated in Figure

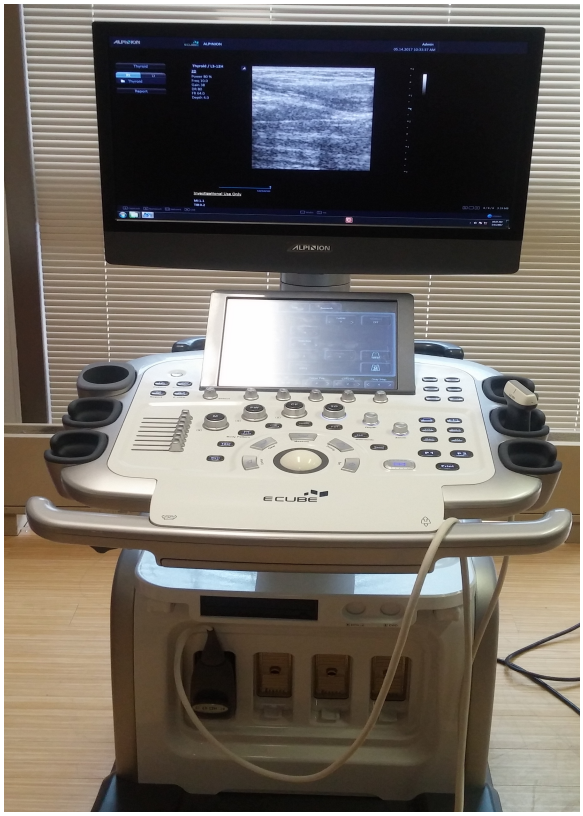

Figure 1.1: An Alpinion E-CUBE 12R ultrasound system.

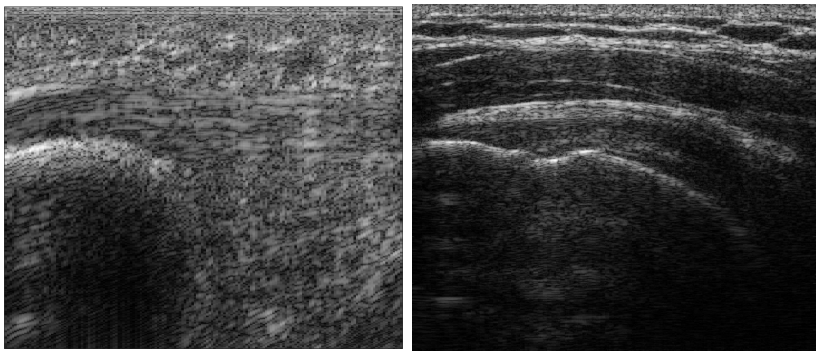

(a) Patellar tendon (b) Rotator cuff

Figure 1.2: Ultrasound images.

1.2. (a) is an ultrasound image of patellar tendon of the knee and (b) shows a rotator cuff tendon ultrasound image.

Different medical applications use different probes. Indeed, the shape of face (footprint) and

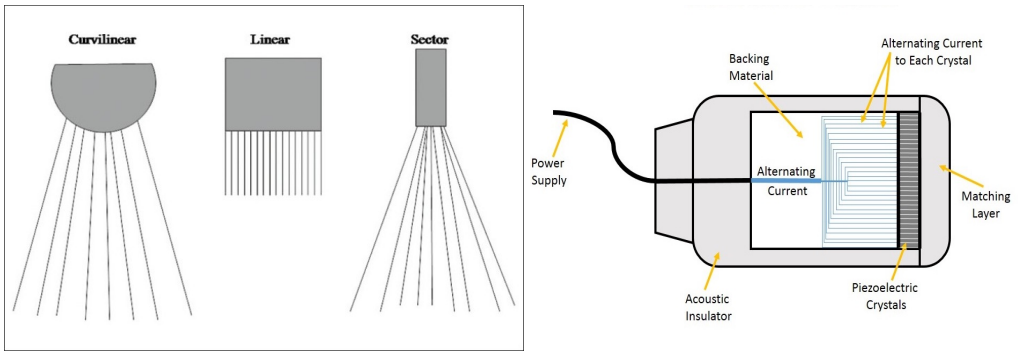

(a) Ultrasound Transducers (b) Transducer Basics

Figure 1.3: Ultrasound Transducers.
(a), Image courtesy of: (Abu-Zidan et al., 2011), (b), Image courtesy of: https://pics-about-space.com/

frequency of the probe specify the transducer performance. The resolution of the image and wave penetration depth are dependent to the frequency of the produced acoustic wave. On the other hand, the probe field of view is connected to its shape. The most utilizable probes are linear, curvilinear, and phased array (sector) probes (Figure 1.3, (a)). A linear probe works with high frequency waves, and consequently provides high resolution images of structures near the body surface. The generated ultrasound images on the screen are generally in rectangular shape (Figure 1.2, (a)). The usage of this probe is in superficial imaging such as: vascular system, skin and soft tissue, musculoskeletal structures, testicular assessment, interstitial fluid diagnosis, ocular ultrasound, breast and thyroid imaging. Curvilinear probe employs lower frequency letting the sound penetrate deeper. It produces pie shaped images, and also has wide field of view due to its curved shape which is ideal for intra-abdominal imaging and organ diagnosis. Phased array probe generates slice of pie shaped images (Figure 1.4). It has small footprint and a wide field of view at the deep parts using low frequency. These features make it compatible for imaging the cardiac structures in the chest through a small acoustic window between the ribs, transesophageal applications, and brain diagnosis.

Emission of ultrasound waves from the probe can be either interrupted or continuous. Interrupted emission results in the brightness mode (B-mode) images (Figure 1.2). In B-mode ultrasound, a 2D image is produced on the screen while the transducer simultaneously scans a plane

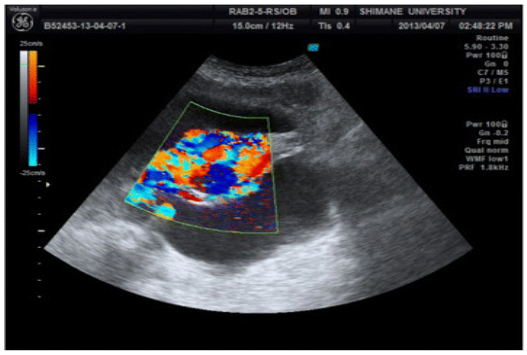

Figure 1.4: Ultrasound doppler image of the blood flow.
Image courtesy of: (Sato et al., 2015)

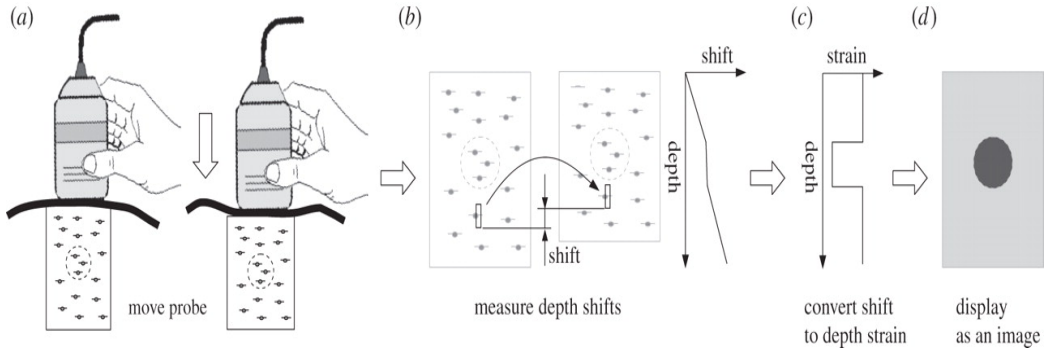

Figure 1.5: Quasi-static procedure.
Image courtesy of (G. Treece et al., 2011)

through the body. However, continuous emission generates Doppler mode that is ideal for mesurment of blood velocity utilizing the Doppler effect as shown in Figure 1.4.

1.2 Ultrasound Elastography

Elastography performs tissue characterization and measurement of the elastic properties of the tissue. In fact, mechanical stress caused by a probe (external) or ultrasonic radiation force (internal) is applied to the tissue. Local tissue deformation is calculated which provides the information about mechanical properties of the tissue. So, it can recognize healthy from unhealthy tissue through

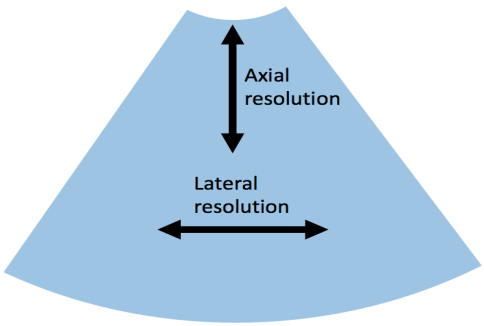

Figure 1.6: Axial and lateral resolution on the image produced by a sector scanner.

stiffness measurements. The most noted ultrasound elastography techniques are: Quasi-static Elastography, Shear Wave Elasticity Imaging (SWEI), Supersonic Shear Imaging (SSI), Acoustic Radiation Force Impulse imaging (ARFI), and Transient Elastography (Bamber et al., 2013; Gennisson, Deffieux, Fink, & Tanter, 2013; Tanter & Fink, 2014). In this thesis, we focus on quasi-static elastography or stain imaging. In Figure 1.5, an approximately static force is applied on the tissue by the probe moving continuously with low velocity. Before and after compression images are compared using a tracking method. The shifts between the locations of the samples in pre- and post-compression images are calculated and stored as the displacement map. Consider the overall change in axial length of tissue as dz. Thus, the post compression time is $\frac{2dz}{c}$. Local axial strain can be calculated as: $S_n = \frac{t_{n+1}-t_n}{\frac{2dz}{c}}$ where t_n is the time shift for segment or time window n. Similarly, the 2D strain can be calculated for the lateral direction. Axial and lateral ultrasound image resolution are different. Thus, the axial strain holds better quality than the lateral one. For axial direction, the resolution is defined as the shortest distance of two distinguishable structures lying in the beam axis that depends mainly on sampling frequency. However, the lateral resolution determined by the beam width and refers to shortest distance of two distinguishable structures which are perpendicular to the beam axis (Figure 1.6).

The general objective of this thesis is to estimate the displacement field between two ultrasound frames through minimizing a regularized cost function. The cost function incorporates both similarity of RF data intensity and displacement continuity. The regularization coefficients are the elastography parameters which can be tuned in the presettings of the ultrasound machine based

on the application. For every organ, these parameters can be determined by visually inspecting the displacement map. The higher or lower regularization weights are employed to improve noisy displacement map or oversmoothed one, respectively. Finally, we are able to calculate the displacement field between two ultrasound images and subsequently find the corresponding strain images revealing mechanical properties of the tissue. The obtained strain images can be used to uncover the invisible tumors and lesions in the initial B-mode images. Furthermore, the strain field is represented by arrows using magnitude and direction of the strain for every point in the image. It clarifies how the tissue actually stretches and in what areas there are more tension as we expect in reality. The method is tested on liver, patellar tendon and Medial Collateral Ligament (MCL) data.

This thesis is organized as follows. In Chapter 2, we will propose a novel technique called GLUE: GLobal Ultrasound Elastography (Hashemi & Rivaz, 2017). We show that GLUE outperforms state of the art ultrasound elastography methods using simulation, phantom and in-vivo experiments. In Chapter 3, we propose an efficient method to find an approximate displacement map between ultrasound images. We refer to this technique as ATME: Affine Transformation Model Elastography (Hashemi, Boily, Martineau, & Rivaz, 2017). We show that ATME efficiently estimates an approximate displacement field using phantom and *in-vivo* experiments. We conclude this thesis in Chapter 4 with a summary and avenues for future work.

Chapter 2

Global Time-Delay Estimation in Ultrasound Elastography

2.1 Introduction

As briefly mentioned in the introduction chapter, ultrasound elastography reveals viscoelastic properties of tissue, which are often correlated with pathology, and is therefore of significant clinical importance. Elastography has evolved into several different techniques, but it can broadly be grouped into dynamic and quasi-static elastography (Gennisson et al., 2013; Hall et al., 2011; Ophir et al., 1999; Parker, Doyley, & Rubens, 2012; Tang, Cloutier, Szeverenyi, & Sirlin, 2015; G. Treece et al., 2011). Dynamic elastography techniques include shear wave imaging (Bercoff, Tanter, & Fink, 2004) and acoustic radiation force imaging (Nightingale, Soo, Nightingale, & Trahey, 2002), which generate deformation in the tissue using ultrasound and provide quantitative mechanical properties of tissue. This work focuses on quasi-static elastography, and more particularly on free-hand palpation elastography, wherein tissue deformation is slow and is generated by slowly palpating the tissue with the hand-held ultrasound probe.

Free-hand elastography and shear wave elastography each has its own strengths. Free-hand strain imaging does not provide quantitative elasticity measures, unless it is combined with an inverse problem approach (Babaniyi, Oberai, & Barbone, 2017; M. Doyley, 2012; Goksel, Eskandari, & Salcudean, 2013; Hoerig, Ghaboussi, Fatemi, & Insana, 2016; Mousavi, Sadeghi-Naini, Czarnota,

& Samani, 2014) that solves for tissue elasticity, whereas shear-wave elastography techniques provide quantitative values of tissue elasticity or shear moduli (Catheline, Wu, & Fink, 1999; Song et al., 2012; Tanter et al., 2008). An advantage of freehand strain imaging emanates from the larger displacement fields compared to that of shear-wave elastography, which can lead to less noise in the estimated displacement field. Although elastography techniques vary significantly in the way they generate tissue deformation and in the biomechanical property they investigate, they all require estimation of tissue displacement, commonly referred to as Time-Delay Estimation (TDE) using ultrasound radio-frequency (RF) signal. TDE is challenging and an active field of research due to various sources of noise and signal decorrelation. In this thesis, we focus on TDE in freehand palpation elastography (M. M. Doyley, Bamber, Fuechsel, & Bush, 2001; Hall, Zhu, & Spalding, 2003; Hiltawsky et al., 2001; Lindop, Treece, Gee, & Prager, 2006; Ophir, Cespedes, Ponnekanti, Yazdi, & Li, 1991; Yamakawa et al., 2003). This approach is attractive as it works with traditional ultrasound machines and does not require any additional hardware.

Window-based techniques calculate TDE for small windows (segments) of the RF data, and can be categorized into amplitude- and phased-based. Amplitude-based methods maximize cross correlation or normalized cross correlation (NCC) (Lopata et al., 2009; Nahiyan & Hasan, 2015; Pan et al., 2015; Zahiri & Salcudean, 2006), whereas phase-based methods find the zero-crossing of the phase of the cross correlation (Ara et al., 2013; X. Chen, Zohdy, Emelianov, & O'Donnell, 2004; Lindop, Treece, Gee, & Prager, 2008; O'Donnell, Skovoroda, Shapo, & Emelianov, 1994; Pesavento, Perrey, Krueger, & Ermert, 1999; Yuan & Pedersen, 2015). Window-based displacement estimation techniques can also be categorized by the dimensionality of the search range: 1D methods only search in axial directions (Bilgen & Insana, 1996; Dickinson & Hill, 1982; Ophir et al., 1991), and 2D techniques perform a search in both axial and lateral directions (Ebbini, 2006; Friemel, Bohs, & Trahey, 1995; Konofagou & Ophir, 1998; G. M. Treece, Lindop, Gee, & Prager, 2008). Since the underlying displacement field is usually 3D, 2D displacement estimation techniques generally outperform their 1D counterparts. The importance of 2D displacement estimation is twofold: it provides more accurate estimates of axial strain (Jiang & Hall, 2015), and it can be used for reconstruction of tissue elastic properties (Babaniyi et al., 2017; M. Doyley, 2012; Goksel et al., 2013; Hoerig et al., 2016; Mousavi et al., 2014). One of the disadvantages of

window-based methods is their sensitivity to signal decorrelation, which can be caused by small out-of-plane motion of the probe or large deformations. Larger windows, approximately of the size 10 ultrasound wavelengths or larger (H. Chen, Shi, & Varghese, 2007; Grondin, Wan, Gambhir, Garan, & Konofagou, 2015), provide more information and hence reduce the estimation variance, but they result in significant signal decorrelation and also decrease the spatial resolution. Remedies for these problems have been proposed such as warping the data (Alam & Ophir, 1997; Alam, Ophir, & Konofagou, 1998; Chaturvedi, Insana, & Hall, 1998), which are generally computationally expensive.

An attractive alternative approach to correlation-based methods is minimization of a regularized cost function (Brusseau, Kybic, Déprez, & Basset, 2008; Hall et al., 2011; Kuzmin, Zakrzewski, Anthony, & Lempitsky, 2015; Maurice & Bertrand, 1999; Pellot-Barakat, Frouin, Insana, & Herment, 2004; Rivaz et al., 2008). These methods exploit the prior information that tissue deformation is smooth, and therefore are robust to signal decorrelation. A disadvantage of these methods is their computational complexity, and as such, they are not readily suitable for real-time implementation. Our group proposed a real-time technique for estimating fine subpixel tissue displacement maps using Dynamic Programming and Analytic Minimization (DPAM) of a regularized cost function (Rivaz et al., 2011; Rivaz, Boctor, Choti, & Hager, 2014), whereby displacements of all the samples in an RF-line are estimated simultaneously. This simultaneous estimation results in both more robust and accurate displacement estimates compared to NCC-based methods that only utilize data within a window. In (Rivaz et al., 2011), the subpixel displacement of a seed-line is calculated first, and is used as an initial estimate for neighboring RF-lines. This algorithm, however, has three drawbacks. First, the simultaneous estimation is limited to individual RF-lines, thereby only utilizing a small fraction of the information available from the entire image. Second, displacement estimates are discontinuous between adjacent RF-lines, creating artifacts in the form of vertical streaks in the strain image. And third, displacement estimation in each line depends on the initial estimate, i.e. the displacement of the previous RF-line. Hence, if there is large decorrelation or noise in an RF-line that results in failure of its displacement estimation, the erroneous displacement propagates to the consequent RF-lines. We present herein a novel method for estimating accurate 2D displacement maps wherein the displacement of the entire image is estimated simultaneously.

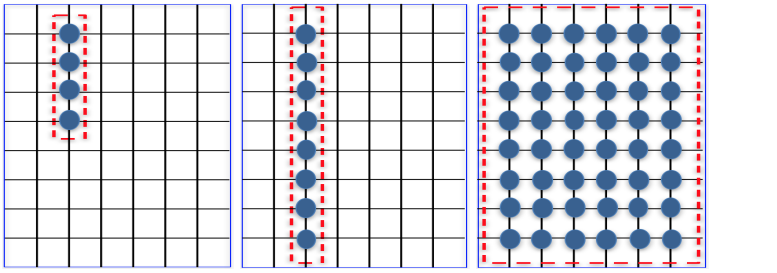

(a) NCC: displacement of windows are estimated independently

(b) DPAM: displacement of entire RF-line is estimated independently

(c) GLUE: displacement of all RF-lines are estimated simultaneously

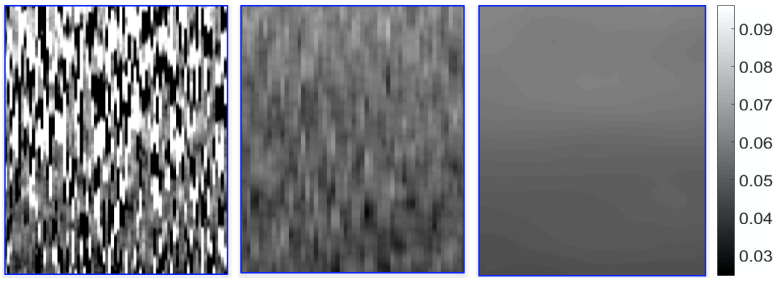

(d) NCC strain

(e) DPAM strain

(f) GLUE strain

Figure 2.1: Comparison of NCC, DPAM and GLUE algorithms, with the corresponding strain images in the second row. In (a) to (c), each circle shows an RF sample that is utilized in TDE. Each grid point corresponds to a sample in RF data. Few samples are shown here to ease visualization; real RF data contains significantly more samples. In (a), few samples are grouped together to form a window, which is used to calculate NCC. The displacement of all samples in an entire RF-line in DPAM (b) or the entire image in GLUE (c) are estimated together. (d) to (f) show strain images of a homogeneous phantom. Note that the average strain is 8%. GLUE substantially outperforms both NCC and DPAM by utilizing all data in the RF-frame.

We call the new method GLobal Ultrasound Elastography (GLUE). Figure 2.1 provides a schematic comparison of three different methods:

(a) Window-based methods, which calculate the displacements of each correlation window independently typically of the size about 50 samples.

(b) DPAM, which uses the information of an RF-line typically of the size about 1000 samples, to acquire the displacements of all samples of the RF data.

(c) GLUE, which utilizes the information of all image samples typically of the size $1000 \times 100 = 10^5$, and calculates TDE of all the samples of the RF frame simultaneously.

GLUE calculates the axial and lateral displacements of all samples of RF data by minimizing a non-linear cost function. Therefore, for a typical RF frame of size 1000×100, there are 2×10^5 variables in the cost function. Typical optimization methods can be intractable in terms of both processing and memory requirements. We convert the optimization problem into a system of equations which entails solving a sparse linear system, and as such, is computationally efficient. We show that our method substantially outperforms previous work using simulation, phantom and *in-vivo* liver data. An executable implementation of GLUE can be found at `https://users.encs.concordia.ca/~hrivaz/Ultrasound_Elastography/`.

The *in-vivo* data in this thesis is obtained from patients with liver tumor who underwent radiofrequency (RF) ablation surgery. Qualitative and quantitative imaging techniques for staging of liver diseases have been implemented on ultrasound, computed tomography (CT), and magnetic resonance imaging (MRI) scanners to address the limitations of liver biopsy. Among these techniques, ultrasound elastography is the most widely used clinically (Petitclerc, Sebastiani, Gilbert, Cloutier, & Tang, 2016). Liver stiffness estimated by elastography techniques is used to evaluate the severity of the underlying chronic liver disease, guide treatment decision, assess disease outcome, and evaluate response to therapy (Tang et al., 2015).

2.2 Methods

In this section, we first briefly describe the closely related previous work (Rivaz et al., 2011). We then present GLUE, and derive equations that enable us to globally calculate TDE of all samples of the RF data simultaneously.

2.2.1 Dynamic Programming Analytic Minimization (DPAM)

Let I_1 and I_2 be images of size $m \times n$ corresponding to before and after some deformation. In DPAM (Rivaz et al., 2011), first the initial integer displacement estimates in the axial (a_i) and lateral (l_i) directions are calculated using dynamic programming (DP) for all $i = 1, \cdots, m$ samples of an RF-line, which is called a seed-line. DP only provides integer displacement estimates, which are not accurate enough for elastography. Therefore, by minimizing the following regularized cost

function, the subsample Δa_i and Δl_i values are calculated such that the duple $(a_i + \Delta a_i, l_i + \Delta l_i)$ gives the axial and lateral displacements at the sample i of the seed-line:

$$\begin{aligned} &C_s(\Delta a_1, \cdots, \Delta a_m, \Delta l_1, \cdots, \Delta l_m,) = \\ &\textstyle\sum_{i=1}^{m}\{[I_1(i,s) - I_2(i + a_i + \Delta a_i, s + l_i + \Delta l_i)]^2 \\ &+\alpha(a_i + \Delta a_i - a_{i-1} - \Delta a_{i-1})^2 \\ &+\beta_a(l_i + \Delta l_i - l_{i-1} - \Delta l_{i-1})^2 \\ &+\beta'_l(l_i + \Delta l_i - l_{i,s-1})^2\} \end{aligned} \tag{1}$$

where s indicates the lateral position of the seed RF-line (i.e. A-line number). The regularization weight α determines how close the axial displacement of each sample should be to its neighbor on the top, and the weights β_a and β'_l determine how close lateral displacement of each sample should be to its neighbors on the top and left. The displacement of the rest of the lines is calculated similar to the seed-line, except that the initial displacements are set to that of the previous line (instead of DP). Since we perform the calculations for one RF-line at a time, we drop the index s to simplify the notations: a_i , l_i , Δa_i and Δl_i are in fact $a_{i,s}$, $l_{i,s}$, $\Delta a_{i,s}$ and $\Delta l_{i,s}$. Using 2D Taylor expansion of the data term in (2) around $(i + a_i, j + l_i)$ gives:

$$I_2(i + a_i + \Delta a_i, j + l_i + \Delta l_i) \approx I_2(i + a_i, j + l_i) + \Delta a_i I'_{2,a} + \Delta l_i I'_{2,l} \tag{2}$$

where $I'_{2,a}$ and $I'_{2,l}$ are the derivatives of the I_2 at point $(i + a_i, j + l_i)$ in the axial and lateral directions respectively. The optimal $(\Delta a_i, \Delta l_i)$ values occur when the partial derivatives of C_s with respect to both Δa_i and Δl_i are zero. Setting $\frac{\partial C_s}{\partial \Delta a_i} = 0$ and $\frac{\partial C_s}{\partial \Delta l_i} = 0$ for $i = 1, \cdots, m$ and stacking the $2m$ unknowns in $\Delta d = [\Delta a_1\ \Delta l_1\ \Delta a_2\ \Delta l_2\ \cdots\ \Delta a_m\ \Delta l_m]^T$ and the $2m$ initial estimates in $d = [a_1\ l_1\ a_2\ l_2 \cdots\ a_m\ l_m]^T$ (Rivaz et al., 2011):

$$A\Delta d = b, \tag{3}$$

where A is a coefficient matrix of size $2m \times 2m$, and b is a vector of length $2m$. An important characteristic of A is that it is penta-diagonal. Therefore, we used the Thomas algorithm (Thomas, 1949) in DPAM to efficiently optimize Eq 3. In summary, solving Eq. 3 provides TDE for all

samples of an RF-line, and for each A-line, this equation is solved independently. We now propose GLUE, a new technique that provides TDE of all RF samples within an image.

2.2.2 Global Time-Delay Estimation (GLUE)

Similar to DPAM, GLUE calculates TDE by optimization of a cost function that incorporates both amplitude similarity and displacement continuity. The difference is that GLUE cost function is formulated for the entire image instead of a single RF-line. In GLUE, we use Taylor expansion similar to DPAM to arrive at a linear system of equations similar to Eq. 3. However, as we will elaborate, the coefficient matrix will not become penta-diagonal, and therefore, the linear system of equations cannot be efficiently solved using traditional methods such as the Thomas algorithm (Thomas, 1949). We will therefore borrow an efficient optimization method from the big data field. The outline of our proposed technique is as follows:

(1) Estimation of integer displacements using DP (Rivaz et al., 2008).

(2) Refinement of DP estimates using GLUE.

(3) Strain estimation by spatially differentiating the displacement field.

We now elaborate the second step, which is the main contribution of this work. Let DP initial estimates be $a_{i,j}$ and $l_{i,j}$. Our cost function is

$$\begin{aligned}
&C(\Delta a_{1,1}, \cdots, \Delta a_{m,n}, \Delta l_{1,1}, \cdots, \Delta l_{m,n}) = \\
&\textstyle\sum_{j=1}^{n} \sum_{i=1}^{m} \{[I_1(i,j) - I_2(i + a_{i,j} + \Delta a_{i,j}, j + l_{i,j} + \Delta l_{i,j})]^2 \\
&+\alpha_1 (a_{i,j} + \Delta a_{i,j} - a_{i-1,j} - \Delta a_{i-1,j})^2 \\
&+\beta_1 (l_{i,j} + \Delta l_{i,j} - l_{i-1,j} - \Delta l_{i-1,j})^2 \\
&+\alpha_2 (a_{i,j} + \Delta a_{i,j} - a_{i,j-1} - \Delta a_{i,j-1})^2 \\
&+\beta_2 (l_{i,j} + \Delta l_{i,j} - l_{i,j-1} - \Delta l_{i,j-1})^2\}
\end{aligned} \tag{4}$$

where α and β are regularization terms for axial and lateral displacements respectively. Note that this function has mn variables of $\Delta a_{i,j}$ and mn variables of $\Delta l_{i,j}$, resulting a total of $2mn$ variables. The first difference between this equation and Eq. 1 is that here, data in all samples are exploited

to in the right hand side (note two summations here over m and n, compared to one summation in Eq. 1 over only m). The second difference is that the left hand side has $2mn$ variables, compared to $2m$ in Eq. 1. In other words, all samples of the RF data are utilized in the cost function, and the displacement of all samples are calculated simultaneously.

Using 2D Taylor expansion around $(i + a_{i,j}, j + l_{i,j})$, we have

$$\begin{aligned}
&C(\Delta a_{1,1}, \cdots, \Delta a_{m,n}, \Delta l_{1,1}, \cdots, \Delta l_{m,n}) = \\
&\textstyle\sum_{j=1}^{n} \sum_{i=1}^{m} \{[I_1(i,j) - I_2(i + a_{i,j}, j + l_{i,j}) \\
&-\Delta a_{i,j} I'_{2,a} - \Delta l_{i,j} I'_{2,l}]^2 \\
&+\alpha_1 (a_{i,j} + \Delta a_{i,j} - a_{i-1,j} - \Delta a_{i-1,j})^2 \\
&+\beta_1 (l_{i,j} + \Delta l_{i,j} - l_{i-1,j} - \Delta l_{i-1,j})^2 \\
&+\alpha_2 (a_{i,j} + \Delta a_{i,j} - a_{i,j-1} - \Delta a_{i,j-1})^2 \\
&+\beta_2 (l_{i,j} + \Delta l_{i,j} - l_{i,j-1} - \Delta l_{i,j-1})^2\}.
\end{aligned} \tag{5}$$

Since $a_{i,j}$ and $l_{i,j}$ are not integer, interpolation is required to calculate $I'_{2,a}$ and $I'_{2,l}$ at the point $(i + a_{i,j}, j + l_{i,j})$. Setting $\frac{\partial C_{i,j}}{\partial \Delta a_{i,j}} = 0$ and $\frac{\partial C_{i,j}}{\partial \Delta l_{i,j}} = 0$ for $i = 1, \cdots, m$, $j = 1, \cdots, n$, and stacking the $2mn$ unknowns in $\Delta \mathbf{d} = [\Delta a_{1,1}\ \Delta l_{1,1}\ \Delta a_{1,2}\ \Delta l_{1,2} \cdots \Delta a_{1,n}\ \Delta l_{1,n}\ \Delta a_{2,1}\ \Delta l_{2,1}\ \Delta a_{2,2}\ \Delta l_{2,2} \cdots \Delta a_{m,n}\ \Delta l_{m,n}]^T$, and the $2mn$ initial estimates in $\mathbf{d} = [a_{1,1},\ l_{1,1},\ a_{1,2},\ l_{1,2},\ \ldots,\ a_{m,n},\ l_{m,n}]^T$, we have:

$$(H + D)\Delta d = H^* \mu - Dd, \tag{6}$$

where

$$D = \begin{bmatrix}
Q & R & O & O & \ldots & O \\
R & S & R & O & \ldots & O \\
O & R & S & R & \ldots & O \\
\vdots & & \ddots & \ddots & \ddots & \\
O & O & \ldots & R & S & R \\
O & O & \ldots & O & R & Q
\end{bmatrix}, \tag{7}$$

$$Q = \begin{bmatrix} \alpha_1+\alpha_2 & 0 & -\alpha_2 & 0 & 0 & \dots & 0 \\ 0 & \beta_1+\beta_2 & 0 & -\beta_2 & 0 & \dots & 0 \\ -\alpha_2 & 0 & \alpha_1+2\alpha_2 & 0 & -\alpha_2 & \dots & 0 \\ 0 & -\beta_2 & 0 & \beta_1+2\beta_2 & 0 & \dots & 0 \\ 0 & 0 & -\alpha_2 & 0 & \alpha_1+2\alpha_2 & \dots & 0 \\ \vdots & & & & & \ddots & \\ 0 & 0 & 0 & \dots & & \alpha_1+\alpha_2 & 0 \\ 0 & 0 & 0 & \dots & & 0 & \beta_1+\beta_2 \end{bmatrix}, \quad (8)$$

$$S = \begin{bmatrix} 2\alpha_1+\alpha_2 & 0 & -\alpha_2 & 0 & 0 & \dots & 0 \\ 0 & 2\beta_1+\beta_2 & 0 & -\beta_2 & 0 & \dots & 0 \\ -\alpha_2 & 0 & 2\alpha_1+2\alpha_2 & 0 & -\alpha_2 & \dots & 0 \\ 0 & -\beta_2 & 0 & 2\beta_1+2\beta_2 & 0 & \dots & 0 \\ 0 & 0 & -\alpha_2 & 0 & 2\alpha_1+2\alpha_2 & \dots & 0 \\ \vdots & & & & & \ddots & \\ 0 & 0 & 0 & \dots & & 2\alpha_1+\alpha_2 & 0 \\ 0 & 0 & 0 & \dots & & 0 & 2\beta_1+\beta_2 \end{bmatrix}. \quad (9)$$

Q is a pentadiagonal matrix of size $2n \times 2n$, and O is a zero matrix of size $2n \times 2n$ and

$$R = diag(-\alpha_1, -\beta_1, -\alpha_1, -\beta_1, \dots, -\alpha_1, -\beta_1). \quad (10)$$

where $H = diag(h'^2(1) \ \dots \ h'^2(m))$ is a symmetric tridiagonal matrix with

$$h'^2(i) = \begin{bmatrix} {I'_{2,a}}^2 & I'_{2,a}I'_{2,l} \\ I'_{2,a}I'_{2,l} & {I'_{2,l}}^2 \end{bmatrix} \quad (11)$$

blocks on its diagonal entries where $I'_{2,a}$ and $I'_{2,l}$ are the derivatives of the I_2 at the point $(i+a_{i,j}, j+$

$l_{i,j}$) in the axial and lateral directions, and

$$H^* = diag(I'_{2,a}(1,1), I'_{2,l}(1,1), I'_{2,a}(1,2), I'_{2,l}(1,2), \ldots, I'_{2,a}(m,n), I'_{2,l}(m,n))$$

and

$$\mu = [g_{1,1},\ g_{1,1},\ g_{1,2},\ g_{1,2},\ \ldots,\ g_{m,n}]^T, \tag{12}$$

$$g_{i,j} = I_1(i,j) - I_2(i + a_{i,j}, j + l_{i,j}). \tag{13}$$

It is important to note that the coefficient matrix in the left hand side of Eq. 6 is a large matrix of size $2mn \times 2mn$. For a typical RF frame of size 1000×100, this amounts to a matrix of size $200,000 \times 200,000$, which requires 320 GB of memory for storage in double precision floating point format, significantly more than 8 GB that is available in a typical machine. Fortunately, this is a band matrix wherein nonzero elements are confined within a diagonal band of length $4n + 1$, thereby significantly reducing the memory requirement. It is important to compare the size of the diagonal bands in the coefficient matrices of Eq. 3 and 6: 5 for DPAM and $4n + 1$ for GLUE. Hence, it is computationally too demanding to use the Thomas algorithm (Thomas, 1949) as we did in DPAM to solve Eq. 6. Instead, we use the successive over-relaxation (SOR) method (Young, 1971), an iterative algorithm for solving linear systems of equations. SOR is significantly faster than traditional methods especially for systems with many variables. It has been applied to various computationally expensive problems such as low-rank factorization (Wen, Yin, & Zhang, 2012), support vector machines (Shao, Zhang, Wang, & Deng, 2011) and computational vision (Szeliski, 2012).

Once the displacement field is estimated, it is common to estimate its spatial gradient to generate strain images. We consider several displacement measurements and perform a least square regression to calculate the strain image. The smoothness of the strain is obtained from the analytic formulation of the cost function which incorporates the displacement continuity in axial and lateral directions, and the regularization coefficients make it possible to adjust the smoothness to the desired level.

2.3 Experiments and Results

In this section, we present results of simulation, phantom and *in-vivo* experiments. Our implementation of the proposed method in MATLAB takes approximately 0.7 sec on a 4^{th} generation 3.6 GHz Intel Core i7 to estimate the 2D displacement fields of size 1000×100 for an image of the same size. Faster performance can be achieved by using an implementation in MATLAB MEX functions.

In all simulation and phantom experiments, the tunable parameters of the GLUE algorithm are set to $\alpha_1 = 5$, $\alpha_2 = 1$, $\beta_1 = 5$, $\beta_2 = 1$, the tunable parameter of the DP (Rivaz et al., 2008) is $\alpha_{DP} = 0.2$. In the in-vivo ablation experiments, α_1 and β_1 are increased to 20 due to the high level of noise in the RF data. The tunable parameters of the DPAM algorithm are always set to $\alpha = 5$, $\beta_a = 10$, $\beta_l = 0.005$ and T = 0.2 (Rivaz et al., 2011). Ultrasound machines have pre-settings for imaging different organs and applications, and the elastography parameters can also be tuned based on the application. The desired parameters for a new application (breast, thyroid, prostate, etc.) can be obtained by visually inspecting the displacement map: if the map is too noisy or too smooth, the regularization weight should be respectively increased or decreased.

Estimation of lateral displacement is significantly more difficult mainly due to the poor resolution of ultrasound images in this direction, thereby limiting most of the previous work to only calculate axial strain images. Simultaneous estimation of the displacement filed for the entire image, however, allows us to substantially improve the quality of both axial and lateral displacements. Therefore, we calculate both axial and lateral strains in simulation and phantom experiments. The unitless metrics signal to noise ratio (SNR) and contrast to noise ratio (CNR) are used to quantitatively compare the results (Ophir et al., 1999):

$$\text{CNR} = \frac{C}{N} = \sqrt{\frac{2(\bar{s_b} - \bar{s_t})^2}{\sigma_b^2 + \sigma_t^2}},\ \text{SNR} = \frac{\bar{s}}{\sigma} \tag{14}$$

where $\bar{s_t}$ and $\bar{s_b}$ are the spatial strain average of the target and background, σ_t^2 and σ_b^2 are the spatial strain variance of the target and background, and $\bar{s}$ and σ are the spatial average and variance of a window in the strain image respectively. The SNR and CNR are calculated for the results using small windows which are located in approximately uniform regions, and therefore, strain is expected

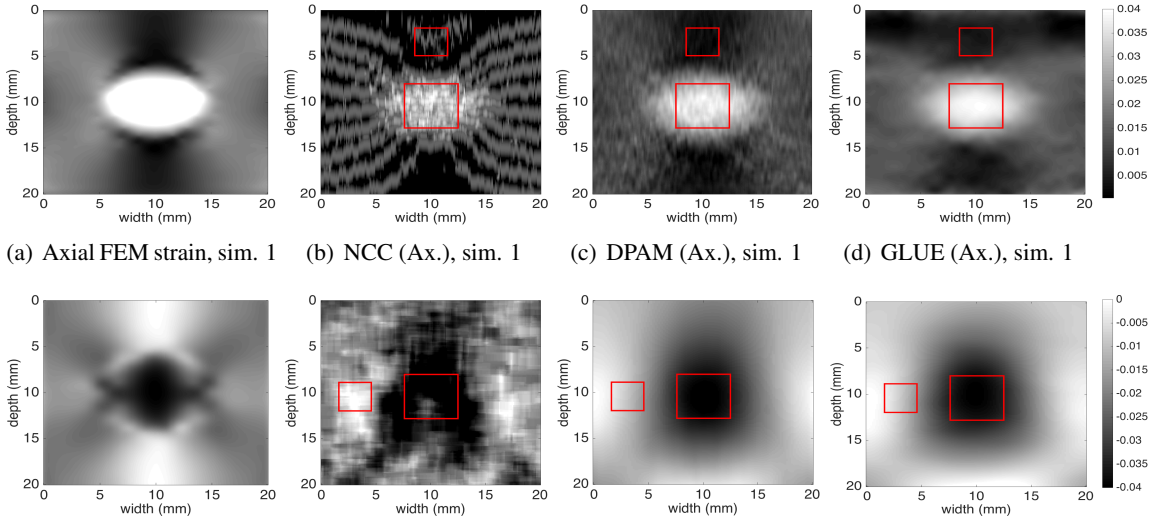

(a) Axial FEM strain, sim. 1 (b) NCC (Ax.), sim. 1 (c) DPAM (Ax.), sim. 1 (d) GLUE (Ax.), sim. 1

(e) Lateral FEM strain, sim. 1 (f) NCC (Lat.), sim. 1 (g) DPAM (Lat.), sim. 1 (h) GLUE (Lat.), sim. 1

Figure 2.2: Field II and FEM simulation results. (a) is the axial ground truth strain. (b) to (d) show the axial strain images of the first simulation. (e) is the lateral ground truth strain. (f) to (h) show the lateral strain images of the first simulation. GLUE substantially outperforms NCC and DPAM in all results. Target and background windows used for CNR calculation are shown in red. The SNR is calculated for the background window.

to be relatively constant within each window.

2.3.1 Simulation Results

Field II software (Jensen, 1996) is used to simulate ultrasound images, and ABAQUS (Providence, RI) software is used to estimate deformations in a digital phantom using finite element method (FEM). The displacement and strain fields are then calculated from the simulated ultrasound images using DPAM and GLUE. For the purposes of comparison, strain images were also calculated using a standard cross correlation method with 80% overlap and a nine point 2D parabolic interpolation to find the 2D sub-sample location of the correlation peak. Figure 2.2 shows the results of the first simulation experiment. The axial and lateral strains are depicted in (a) to (d), and (e) to (h) respectively. (a) and (e) are the ground truth axial and lateral strain images simulated using FEM. The axial strain images obtained by cross correlation, DPAM and GLUE are shown in (b), (c) and (d), respectively. The second row shows the corresponding lateral strains. It is clear that GLUE

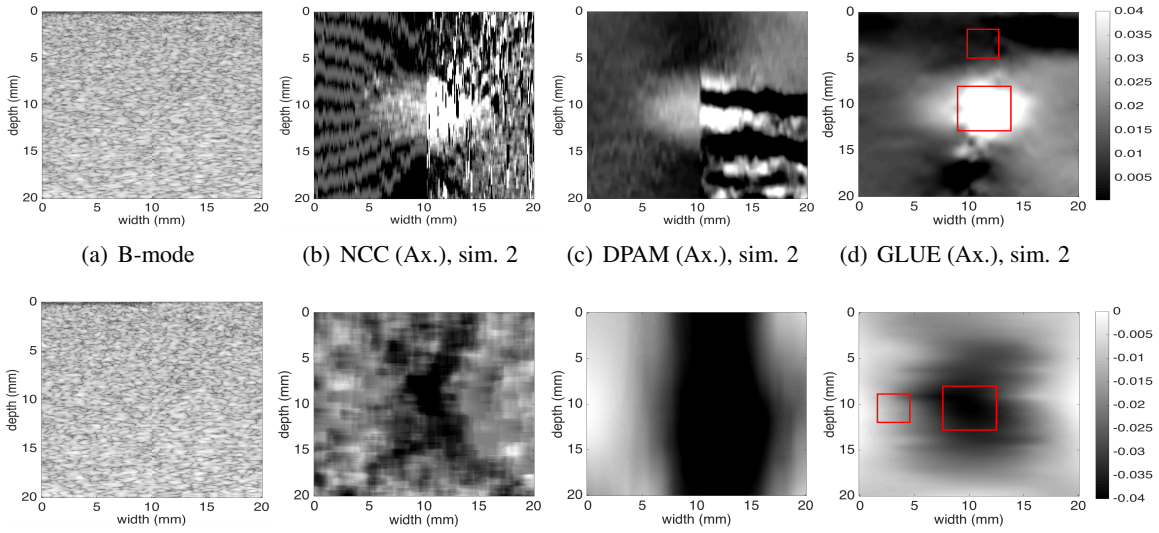

(a) B-mode (b) NCC (Ax.), sim. 2 (c) DPAM (Ax.), sim. 2 (d) GLUE (Ax.), sim. 2

(e) B-mode (f) NCC (Lat.), sim. 2 (g) DPAM (Lat.), sim. 2 (h) GLUE (Lat.), sim. 2

Figure 2.3: Field II and FEM simulation results. A vertical slippage exists in the motion field at the middle of the image. (a) is the first ultrasound image. (b) to (d) are the axial strain images. (e) is the second ultrasound image. (f) to (h) are the lateral strain images. Target and background windows used for CNR calculation of the GLUE results are shown in red. The SNR is calculated for the background window.

significantly outperforms DPAM and NCC in both reducing noise and improving contrast.

In the second simulation (Figure 2.3), we consider tissue slippage which might happen in real world, e.g. at the boundary of different organs such as prostate and rectum (Hoogeman, van Herk, de Bois, & Lebesque, 2005) or for lesions that are not connected to the surrounding tissue. In this experiment, the ultrasound image related to pre-compression is the same as before, whereas a vertical slippage occurs in the second image. The average axial strains to the left and right of the slippage line are respectively 1% and 2%. The strain images generated using cross correlation, DPAM and GLUE are depicted in (b), (c) and (d) for axial strain and (f), (g) and (h) for lateral strain respectively. As one can see, NCC and DPAM fail in this situation while GLUE accurately computes TDE despite the large discontinuity in the underlying deformation field.

The corresponding SNR and CNR values are measured for both simulation experiments. CNR values are calculated between the target (tumor) and background (outside the target) windows each of size 5 mm $\times$ 5 mm and 3 mm $\times$ 3 mm respectively, and are provided in Table 2.1 and Table 2.2. SNR values are also shown in the table, which are calculated for the background windows. GLUE

provides substantially higher SNR and CNR values compared to both NCC and DPAM.

Table 2.1: The SNR and CNR values of the simulation experiment. Target windows (5mm X 5mm) and background windows (3mm X 3mm) used for CNR calculation are shown in Figure 2.2. The SNR is calculated in the background window. Maximum values are in bold font.

	SNR		CNR	
Experiment 1	Axial	Lateral	Axial	Lateral
NCC	2.14	0.52	4.94	7.69
DPAM	5.29	4.50	14.62	10.87
GLUE	**44.63**	**4.61**	**26.31**	**11.03**

Table 2.2: The SNR and CNR values of the simulation experiment. Target windows (5mm X 5mm) and background windows (3mm X 3mm) used for CNR calculation are shown in Figure 2.3. The SNR is calculated in the background window.

	SNR		CNR	
Experiment 2	Axial	Lateral	Axial	Lateral
NCC	Fails	Fails	Fails	Fails
DPAM	Fails	Fails	Fails	Fails
GLUE	43.70	4.41	17.45	6.72

2.3.2 Phantom Results

For experimental evaluation, RF data is acquired from a CIRS elastography phantom (Norfolk, VA) using an Antares Siemens system (Issaquah, WA) at the center frequency of 6.67 MHz with a VF10-5 linear array at a sampling rate of 40 MHz. The results of NCC, DPAM and GLUE methods are shown in Figure 2.4, along with the target and background windows used for SNR and CNR calculation. SNR is only calculated for the background window. The results are summarized in Table 2.3. Again, GLUE substantially improves both SNR and CNR in both axial and lateral strain images.

2.3.3 In-vivo Results

The *In-vivo* data is acquired from four patients undergoing open surgical radiofrequency thermal ablation for primary or secondary liver cancers. This data is collected as follows at Johns Hopkins

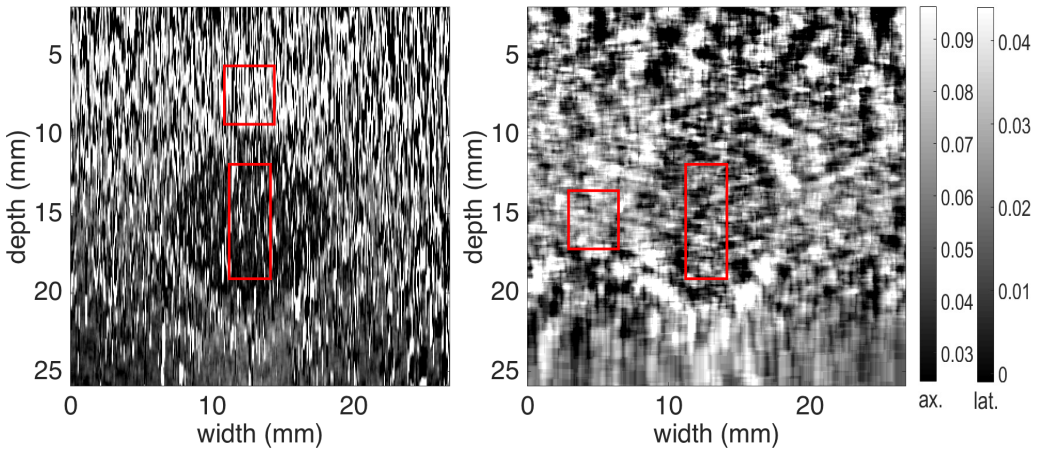

(a) Ax. (NCC) (b) Lat. (NCC)

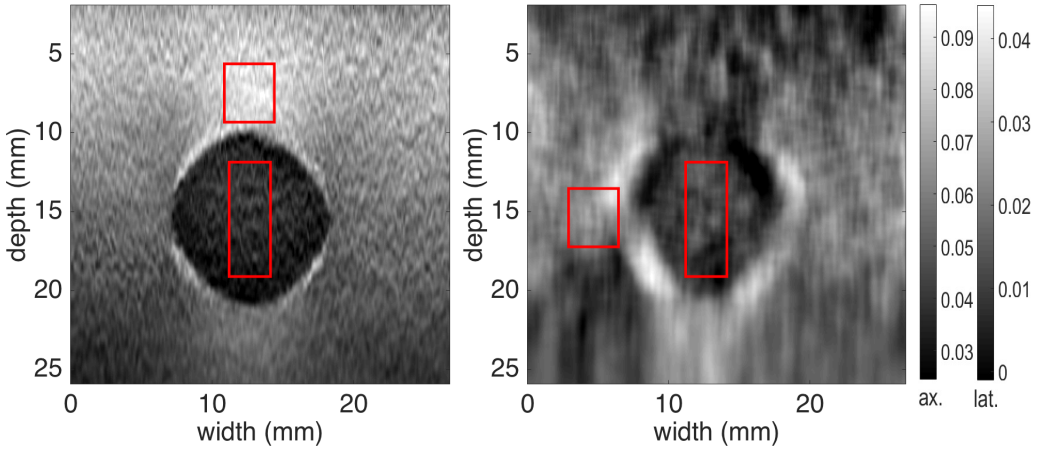

(c) Ax. (DPAM) (d) Lat. (DPAM)

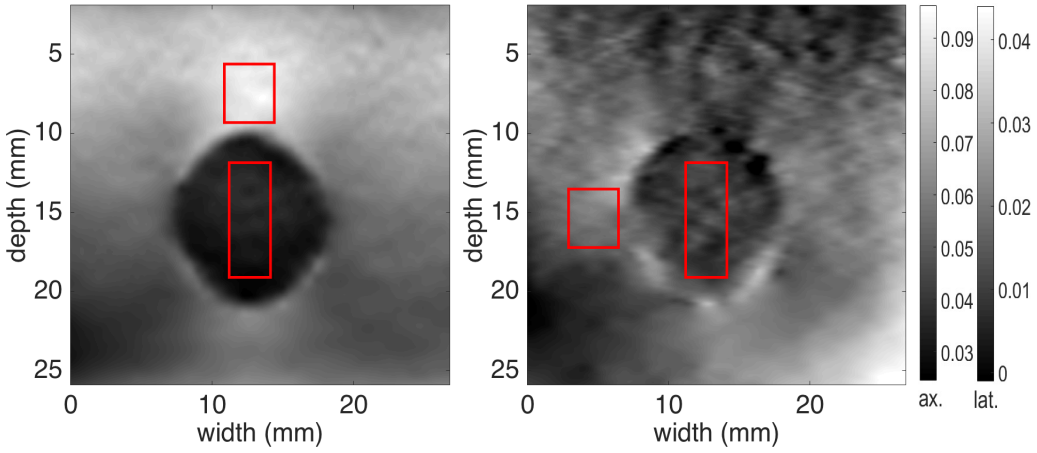

(e) Ax. (GLUE) (f) Lat. (GLUE)

Figure 2.4: Results of the phantom experiment. Axial and lateral strain images as well as the target and background windows (in red) for calculation of SNR and CNR are shown (see Table 2.3 for results). The hard lesion is spherical and has a diameter of 1 cm. The axial and lateral strain scales are identical for NCC, DPAM and GLUE to ease comparison, and are shown in the right column.

Table 2.3: The SNR and CNR of the strain images of the experimental phantom. Target and background windows used for CNR calculation are shown in Figure 2.4. The SNR is calculated for the background window. Maximum values are in bold font.

	SNR		CNR	
	Axial	Lateral	Axial	Lateral
NCC	2.20	3.60	1.07	0.39
DPAM	26.21	4.77	16.01	3.25
GLUE	**29.85**	**7.22**	**18.21**	**4.09**

Table 2.4: The SNR and CNR values of the strain images of the *in-vivo* data in Figure 2.5. The SNR is calculated for the background window of size 6 mm $\times$ 6 mm. Maximum values are in bold font.

	SNR		CNR	
	DPAM	GLUE	DPAM	GLUE
P1	7.94	**56.21**	3.73	**13.64**
P2	3.34	**13.04**	1.46	**12.42**
P3	4.47	**23.29**	5.45	**20.14**
P4	3.22	**10.11**	3.60	**6.62**
average	4.74	**25.66**	3.56	**13.20**
improv. %	-	441	-	271

Hospital: for the first patient, ultrasound RF data is acquired only after ablation. For the second, third, and fourth patients, ultrasound RF data is collected both before and after ablation. Data collection from the tumour involved holding the probe is hard-to-reach locations and angles, which lead to unwanted out-of-plane motions of the probe. In addition, microbubbles and high temperature gradients created by the ablation process add noise in the the RF data. Furthermore, the pulsation of hepatic vessels create complicated deformation fields. Therefore, the pre- and post-compression images suffer from high levels of decorrelation. Traditional NCC failed to estimate the displacement field, and therefore, we only show GLUE and DPAM results in this data.

Figure 2.5 shows B-mode scans, strain images and computed tomography (CT) scans obtained after RF ablation in all four patients. Note that the extent of the ablation is almost completely invisible in B-mode images. The coagulated tissue is clearly visible in strain images, and is marked with red arrows. The CNR values of the ablation lesion are calculated between the target (inside the ablation lesion) and background (outside the target) windows, each of size 6 mm $\times$ 6 mm. The SNR

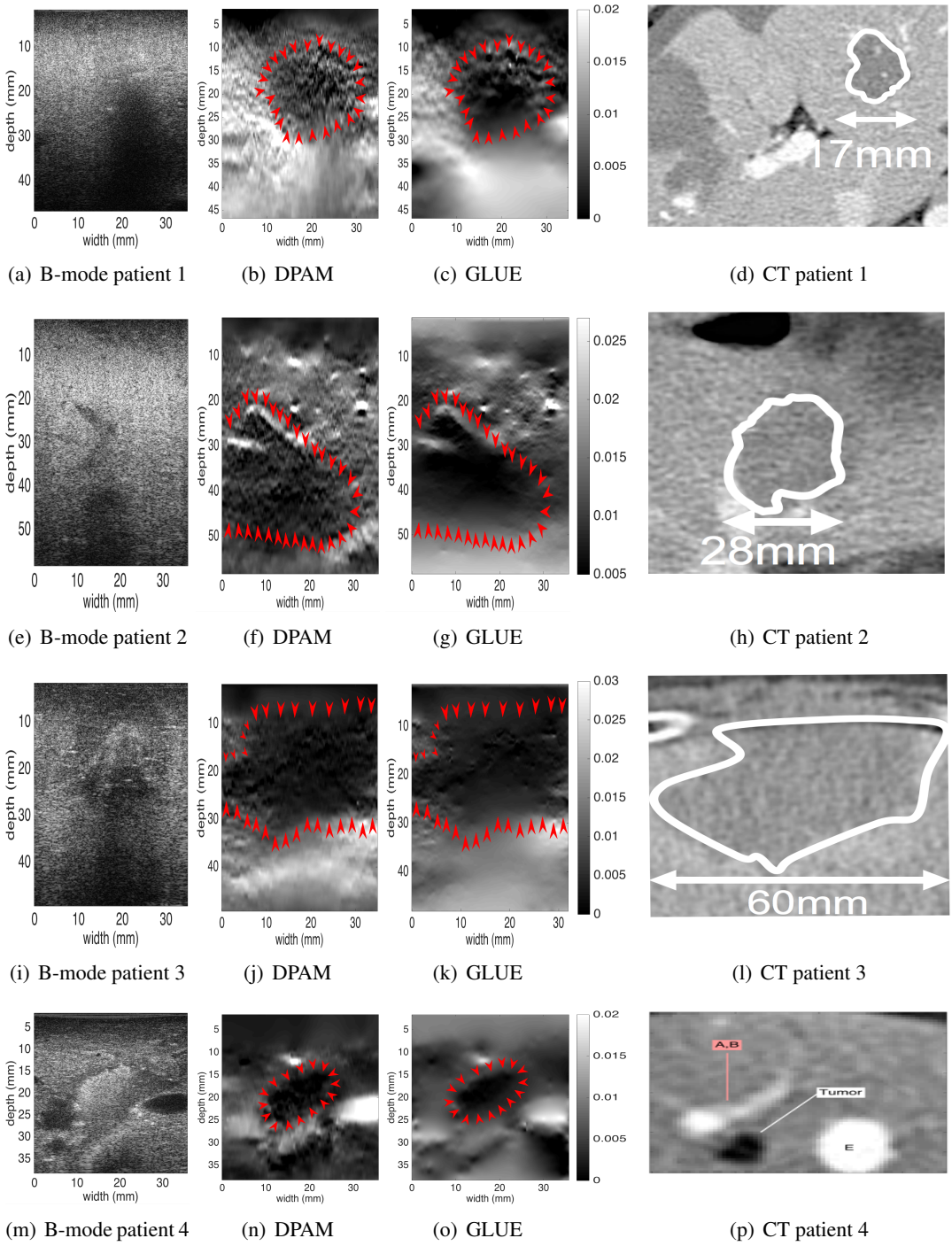

(a) B-mode patient 1 (b) DPAM (c) GLUE (d) CT patient 1

(e) B-mode patient 2 (f) DPAM (g) GLUE (h) CT patient 2

(i) B-mode patient 3 (j) DPAM (k) GLUE (l) CT patient 3

(m) B-mode patient 4 (n) DPAM (o) GLUE (p) CT patient 4

Figure 2.5: *In-vivo* images of the ablation lesion acquired after ablation of liver tumours. Each row corresponds to one patient. The first column shows ultrasound images, and the second and third columns respectively show the results of DPAM and GLUE. The ablation lesion is marked with red arrows, and is clearly visible in strain images. CT images with the delineated ablation lesions are shown in the right column.

Table 2.5: The SNR and CNR of the strain images of the *in-vivo* data in Figures 2.6 and 2.7. The CNR calculated for the target and background window each of size 6mm $\times$ 6mm. The SNR is calculated for the background window. Maximum values are in bold font.

	SNR		CNR	
	DPAM	GLUE	DPAM	GLUE
P2	12.52	**17.71**	11.27	**13.72**
P3	8.39	**30.15**	4.32	**12.92**
P4 (US 1&2)	16.68	**23.23**	2.19	**13.29**
P4 (US 3&4)	9.97	**26.21**	1.38	**14.03**
average	11.89	**24.32**	4.79	**13.49**
improv. %	-	105	-	182

values are calculated for the background windows. Table 2.4 shows that we obtain approximately 5-fold and 4-fold improvements in SNR and CNR respectively by utilizing GLUE method instead of DPAM. The ablation lesion in strain images corresponds well to the post-operative CT images shown in the right column.

Figure 2.6 and 2.7 show pre-ablation results obtained by DPAM and GLUE in second, third and fourth patients. In Figure 2.6, the tumors are marked with red arrows, and are hardly visible in the B-mode images in (a) and (d). The strain images provide a significantly improved contrast between the tumor and healthy tissue. CNR values are calculated between target (inside the tumor) and background (outside the target) windows, each of size 6 mm $\times$ 6 mm. The SNR values are calculated for the background windows (Table 2.5). Again, we see large improvements with GLUE as a result of utilizing all the data in the RF frames.

Figure 2.7 shows the B-mode, strain, and CT images of Patient 4. All images are obtained before ablation. In (a), the tumor is not visible in the B-mode image. A and B are veins which compress easily due to their low pressure. In contrast, C, D (Arteries) and E (middle hepatic vein) pulsate with the heart beat and may have low or high pressure. The probe motion and variations in the diameter is shown in graph (d). Two ultrasound images US 1 and US 2 (see part (d)) are obtained while the vein diameter variation and probe motion are in the same direction due to high blood pressure. Another pair of ultrasound images, US 3 and US 4, are acquired at low blood pressure when they are pointing to the opposite side in graph (d). Thus, we acquired two paired ultrasound frames at two different phases of the heart beat. The result of DPAM and GLUE using US 1 and 2 are shown

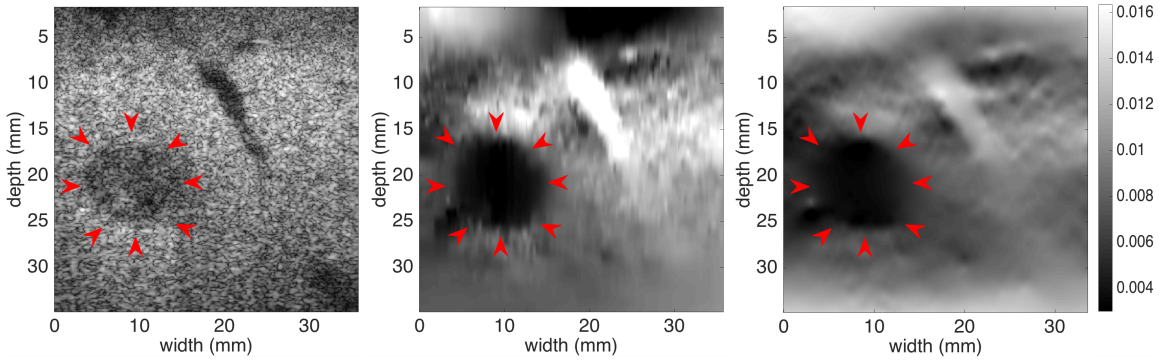

(a) B-mode (b) DPAM (c) GLUE

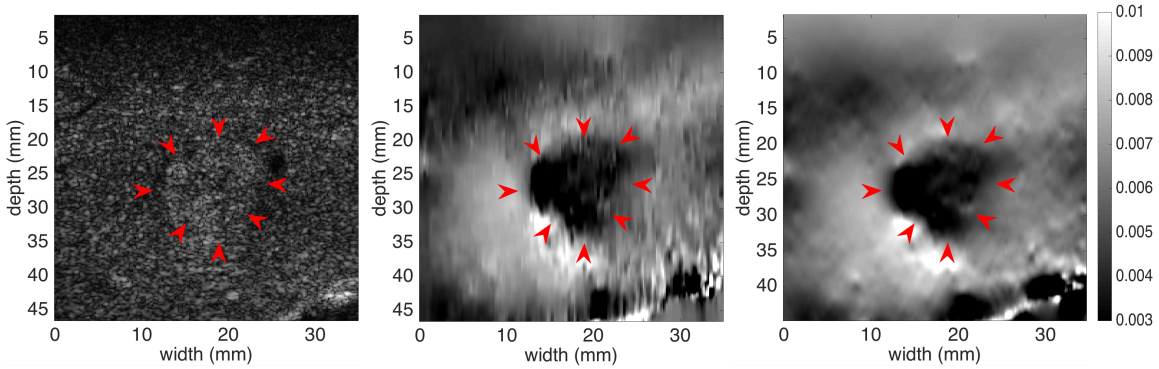

(d) B-mode (e) DPAM (f) GLUE

Figure 2.6: B-mode and strain images of the patient data before ablation. First and second rows respectively correspond to patients 2 and 3. The red arrows point to the tumours. The strain images provide a substantially improved visualization of the tumours compared to the B-mode ultrasound images.

in (b) and (e) respectively. US 3 and US 4 are used to obtain DPAM and GLUE strain images in (c) and (f). It is very interesting to compare the middle hepatic vein (marked as E in (a)) in strain images in the second and third columns: E looks hard in the second column, and soft in the third column. The reason lies in large pulsation of the middle hepatic vein due to heart beats. CT scans corresponding to two different phases of the heart beat are depicted in (g) and (h). Here, A to D mark the same anatomy as (a).

Table 2.5 summarizes the SNR and CNR values of patients 2 to 4. Average values for DPAM and GLUE are shown in the fifth row. GLUE outperforms DPAM by approximately 2-fold and 3-fold improvements in SNR and CNR values.

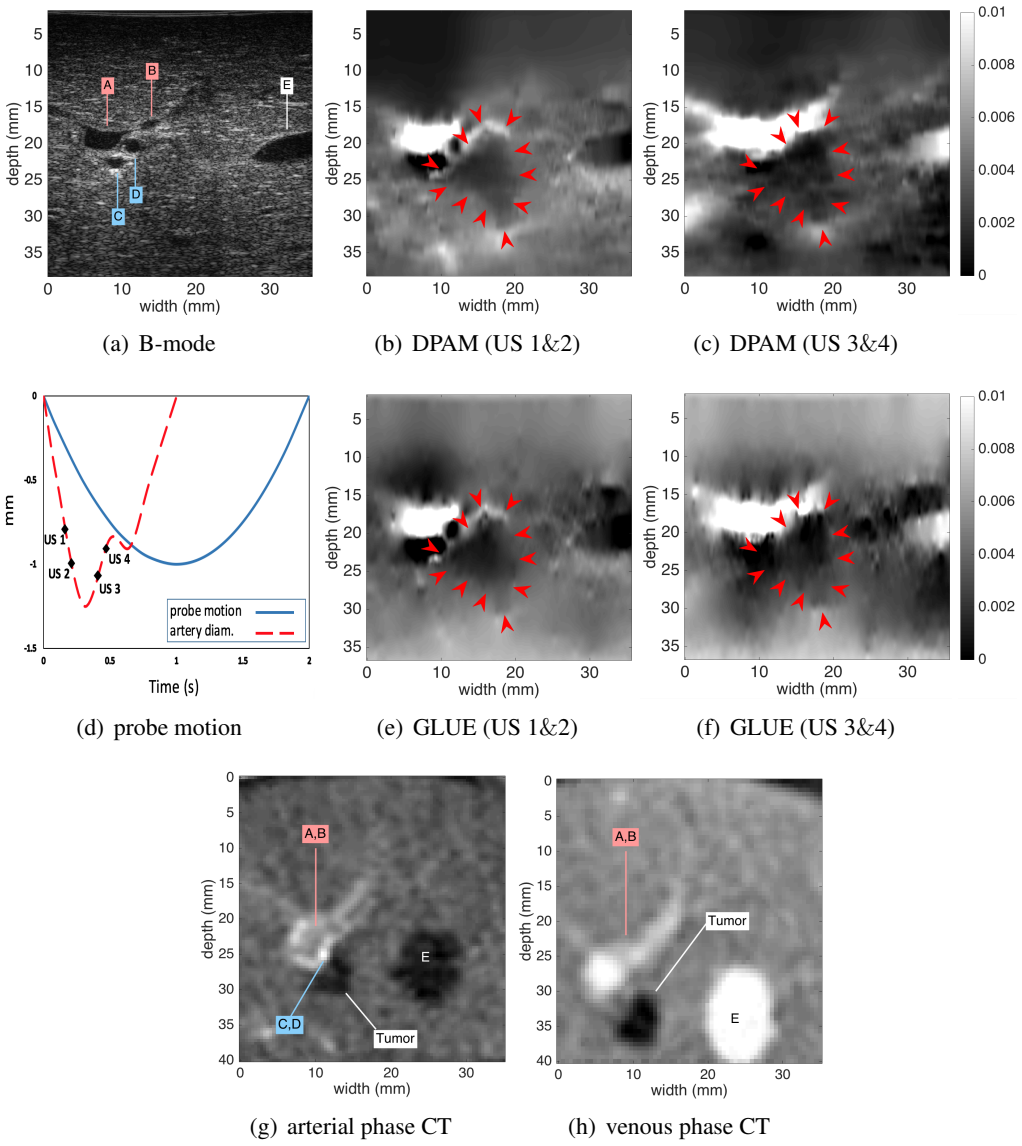

(a) B-mode (b) DPAM (US 1&2) (c) DPAM (US 3&4)

(d) probe motion (e) GLUE (US 1&2) (f) GLUE (US 3&4)

(g) arterial phase CT (h) venous phase CT

Figure 2.7: B-mode and strain images of patient 4 before ablation. (a) shows B-mode image, and (b) and (c) show the strain images from the DPAM method using US 1 and 2 frames (for b) and US 3 and 4 frames (for c). (d) shows the motion of the probe and the variation in the diameter of the arteries due to the heart beat. (e) and (f) show results of the GLUE method. (g) is the arterial phase and (h) is the venous phase contrast CT images. The tumor is marked with red arrows in (b), (c), (e), and (f).

2.4 Discussion

Incorporating the prior information of displacement continuity generally improves the TDE. Window-based methods enforce continuity in a small window, DPAM utilizes continuity in a single RF-line, and GLUE utilizes displacement continuity throughout the image. This is a reason for the improvement from window-based methods to DPAM to GLUE. However, there is also a disadvantage of using prior information, which is rooted in the bias-variance trade-off (Geman, Bienenstock, & Doursat, 1992; Walker & Trahey, 1995). The prior information decreases the variance, but it increases the bias. The increase in the bias can lead to strain images with lower contrast. Nevertheless, the substantial improvement in the CNR shows that GLUE strikes a balance between bias and variance.

In order to image some of the tumors during the intervention, the ultrasound probe had to be held at difficult angles, which lead to unwanted out-of-plane motion of the probe during the palpation. Furthermore, ablation creates microbubbles and high temperature gradients, which add high levels of noise to the RF data. Therefore, the pre- and post-compression images suffer from high decorrelation. An advantage of DPAM and GLUE lies within the simultaneous displacement estimation of several samples and exploitation of the continuity prior. As such, both of these methods generate displacement fields from such noisy data, whereas traditional window-based methods calculate the displacement of each window independently and can fail for decorrelated windows. An example of the output of the traditional NCC-based TDE method on this liver data is shown in (Kuzmin et al., 2015).

The regularization term in the GLUE cost function enforces displacement continuity. The strain field is the spatial derivative of the displacement field, and as such, is piecewise continuous in theory (i.e. strain can be discontinuous). This is in fact desired since the strain field can be discontinuous in the boundary between two different types of tissue. In practice, however, large kernels are commonly used for performing the spatial gradient operation to alleviate noise amplification of the derivative operator. This large kernel guarantees smooth strain fields, but has the disadvantage of blurring the boundary of two different types of tissue. We have proposed Kalman filter (Rivaz et al., 2011) and bilateral filter (Khodadadi, Aghdam, & Rivaz, 2015) to generate piecewise continuous

strain fields that are sharp at the boundary of two different tissue types but are smooth within each type of tissue.

2.5 Conclusion

In this chapter, we introduced GLUE, a novel technique for calculating both axial and lateral displacement fields between two frames of RF data. We estimated the displacement field of the entire image simultaneously, which led to substantial improvement over previous work. An unoptimized implementation of the proposed method in MATLAB takes only 0.7 sec on a typical CPU. Therefore, our technique is highly suitable for implementation in commercial ultrasound systems. An implementation of GLUE is publicly available at `https://users.encs.concordia.ca/~hrivaz/Ultrasound_Elastography/`. In the next chapter, we propose an efficient method to calculate an approximate displacement field for ultrasound elastography.

Chapter 3

Efficient Estimation of Tissue Displacement Using an Affine Transformation Model

3.1 Introduction

In this chapter, we propose a novel technique for efficient and robust estimation of the initial displacement field. The initial estimation of the GLUE framework is performed using DP, which is computationally expensive. We model tissue deformation using a 2D affine transformation to calculate an approximate initial displacement. We call our method ATME: Affine Transformation Model Elastography. Since 2D affine transformation has only six degrees of freedom (DOF), it can be efficiently estimated by minimizing a quadratic error measure. Afterward, regularized global cost function is optimized by using initial displacement fields obtained from the previous step. We convert the optimization problem to a set of equations, which entails solving a sparse linear system, and as such, is computationally efficient.

The importance of the affine transformation model is twofold. First, there are only six parameters to estimate for the total RF frame, which is computationally efficient and suitable for real-time

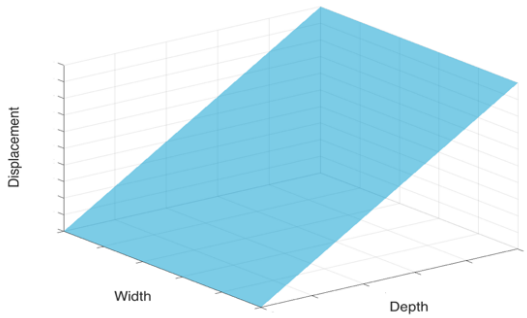

Figure 3.1: Displacement field between a pair of ultrasound images in a uniform tissue.

implementation. Second, the prior information that tissue deformation is relatively planar is utilized. Therefore, this method is able to estimate tissue displacements in the presence of large noise. It is also robust to signal decorrelation by exploiting the prior information that tissue deformation is smooth. This method can be applied to a range of elastography imaging techniques including freehand palpation, wherein tissue is deformed gently using a hand-held ultrasound probe.

The rest of the chapter is organized as follows. We first introduce ATME, and derive the equations for estimation of TDE from RF data. We then show that ATME outperforms previous work using simulation experiments. We then collect RF data from *in-vivo* patellar tendon and medial collateral ligament (MCL) of healthy volunteers, and conclude the chapter by showing that ATME can recover tendon and MCL motion in such challenging data.

3.2 Methods

Let $I_1(i,j)$ and $I_2(i,j)$ be two ultrasound RF frames acquired before and after some tissue deformation, and i and j respectively be samples in the axial and lateral directions. The main idea is to enforce an affine displacement field between the two ultrasound images, such that an approximate initial displacement field can be calculated. This initial displacement field will then be utilized in a cost function that incorporates similarity of RF data intensity, as well as prior information of displacement continuity. Since the initial displacement field is affine, its estimation will be both fast and robust.

To demonstrate why an affine transformation well approximates the underlying deformation

field, assume that the tissue is homogenous and isotropic. In such medium, free-hand palpation ultrasound elastography generates a planar deformation field for both axial and lateral displacements (Fig. 3.1). This planar deformation can be simply formulated using affine transformation, which has only 6 DOF. As such, estimation of this transformation is very efficient. Furthermore, there is a smaller chance of getting trapped in a local minimum. Real tissue is neither homogenous nor isotropic, and therefore, actual deformation is not planar. Therefore, this planar deformation can only be used as an approximation of the true underlying displacement. We use a hierarchal affine transformation model similar to the technique proposed in Ref. (Bergen, Anandan, Hanna, & Hingorani, 1992):

$$\begin{aligned} a(x,y) &= g_1 + g_2 x + g_3 y \\ l(x,y) &= g_4 + g_5 x + g_6 y \end{aligned} \tag{15}$$

where a and l are axial and lateral displacements of a pixel at (x, y) location. The affine parameter g_i can be obtained by minimizing an error function $E(\delta g)$ with respect to an incremental estimate g through an iterative procedure. To formulate E, let , and denote the current estimate of the affine parameter, axial and lateral displacements, respectively. The error function $E(\delta g)$ is defined as:

$$E(\delta g) = \sum_{y=1}^{n} \sum_{x=1}^{m} (\Delta I + (\nabla I)^T X \delta g)^2 \tag{16}$$

where $\Delta I = I_2(x, y) - I_1(x - a^k, y - l^k)$, and ∇I is the gradient of I_1. The matrix X is defined as:

$$D = \begin{bmatrix} 1 & x & y & 0 & 0 & 0 \\ 0 & 0 & 0 & 1 & x & y \end{bmatrix} \tag{17}$$

To simplify the notation of single pixel displacement, we simplify $a(x, y)$ to $a_{i,j}$ and $l(x, y)$ to $l_{i,j}$. Once the initial displacement field is estimated, it can be utilized in the next step. The cost function with the summation on all image pixels is defined as:

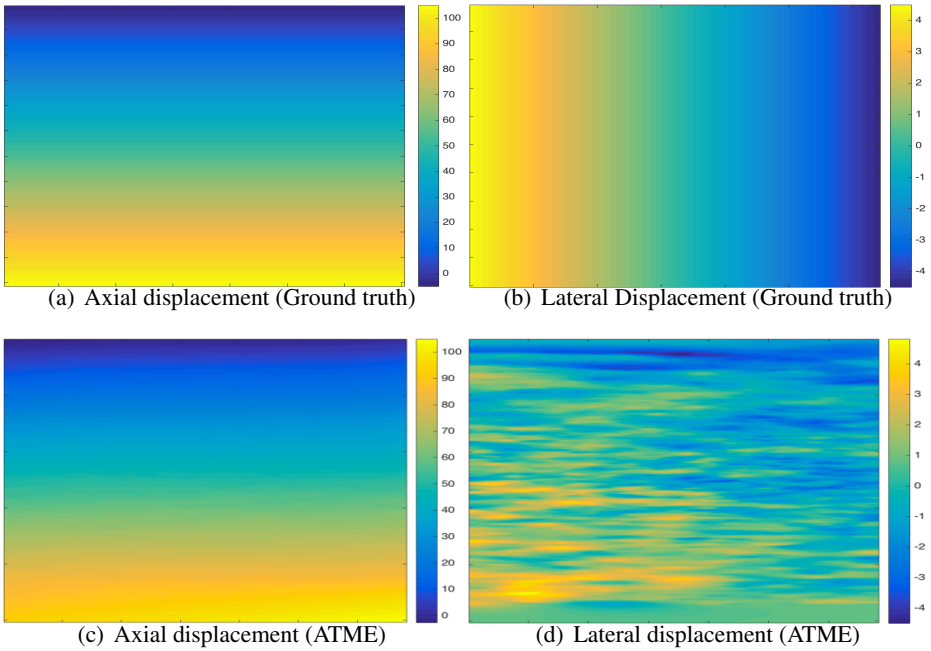

(a) Axial displacement (Ground truth) (b) Lateral Displacement (Ground truth)

(c) Axial displacement (ATME) (d) Lateral displacement (ATME)

Figure 3.2: Field II and finite element simulation results. (a) and (b) show the axial and lateral ground truth displacement images of the simulation experiment. (c) and (d) are the corresponding axial and lateral displacement fields obtained from ATME.

$$
\begin{aligned}
&C(\Delta a_{1,1}, \cdots, \Delta a_{m,n}, \Delta l_{1,1}, \cdots, \Delta l_{m,n}) = \\
&\sum_{j=1}^{n}\sum_{i=1}^{m}\{[I_1(i,j) - I_2(i + a_{i,j}, j + l_{i,j}) - \Delta a_{i,j} I'_{2,a} - \Delta l_{i,j} I'_{2,l}]^2 \\
&+ \alpha_1(a_{i,j} + \Delta a_{i,j} - a_{i-1,j} - \Delta a_{i-1,j})^2 + \beta_1(l_{i,j} + \Delta l_{i,j} - l_{i-1,j} - \Delta l_{i-1,j})^2 \\
&+ \alpha_2(a_{i,j} + \Delta a_{i,j} - a_{i,j-1} - \Delta a_{i,j-1})^2 + \beta_2(l_{i,j} + \Delta l_{i,j} - l_{i,j-1} - \Delta l_{i,j-1})^2\}.
\end{aligned}
\tag{18}
$$

where α and β are regularization terms for axial and lateral displacements respectively. By minimizing the cost function using the initial guess $(a_{i,j}, l_{i,j})$, the sub-sample axial and lateral displacements $(\Delta a_{i,j}, \Delta l_{i,j})$ for the total image are calculated. The initial displacements $(a_{i,j}, l_{i,j})$ provided through the previous step are added to the subsample displacements. This presents us the final lateral and axial displacements i.e. $(a_{i,j} + \Delta a_{i,j}, l_{i,j} + \Delta l_{i,j})$. Once the displacement field is estimated, its spatial gradient is calculated to obtain the strain image.

3.3 Experiments and Results

We tested our proposed method on acquired data from simulation and clinical trials. In this section, we also present results of clinical trials using a previous work, DPAM (Rivaz et al., 2011), to compare with ATME. Estimation of lateral displacement is significantly more difficult mainly due to the poor resolution of ultrasound images in this direction, thereby limiting previous work to only calculate axial strain images. Simultaneous estimation of the displacement filed for the entire image, however, allows us to substantially improve the quality of both axial and lateral displacements.

3.3.1 Simulation Experiments

Field II software (Jensen, 1996) is used to simulate ultrasound images. The phantom is homogenous and isotropic with a Poisson ratio of $\nu = 0.49$. A uniform axial force profile is applied to the top of the phantom to generate 6% axial strain. More than 12 scatterers are randomly distributed in each cubic millimeter of the phantom to generate fully developed speckles. Further details of the data acquisition are available in Ref. (Rivaz et al., 2011). The Axial and lateral ground truth displacements and also the ones obtained by ATME are shown in Fig. 3.2. Note that the tissue is homogenous, and therefore, the deformation is assumed to be planar.

Table 3.1: The SNR and CNR of the strain images of Fig. 3.5. Maximum values are in bold font.

	SNR		CNR	
Experiment	DPAM	ATME	DPAM	ATME
Patellar tendon flexion (distal portion)	4.77	**10.06**	5.46	**11.98**
Patellar tendon flexion (proximal portion)	6.41	**9.17**	**3.51**	3.24
MCL pure valgus	0.7	**4.17**	1.26	**2.16**
MCL pure valgus	3.20	**6.59**	6.28	**10.70**
Average	3.77	**7.50**	4.13	**7.02**

3.3.2 *in-vivo* Experiments

Ethics approval was obtained at both McGill University Health Centre (MUHC) and Concordia University to collect ultrasound images of human subjects. Valgus stress was applied to the knee, and ultrasound data of the MCL was collected during the stress. In the second set of experiments,

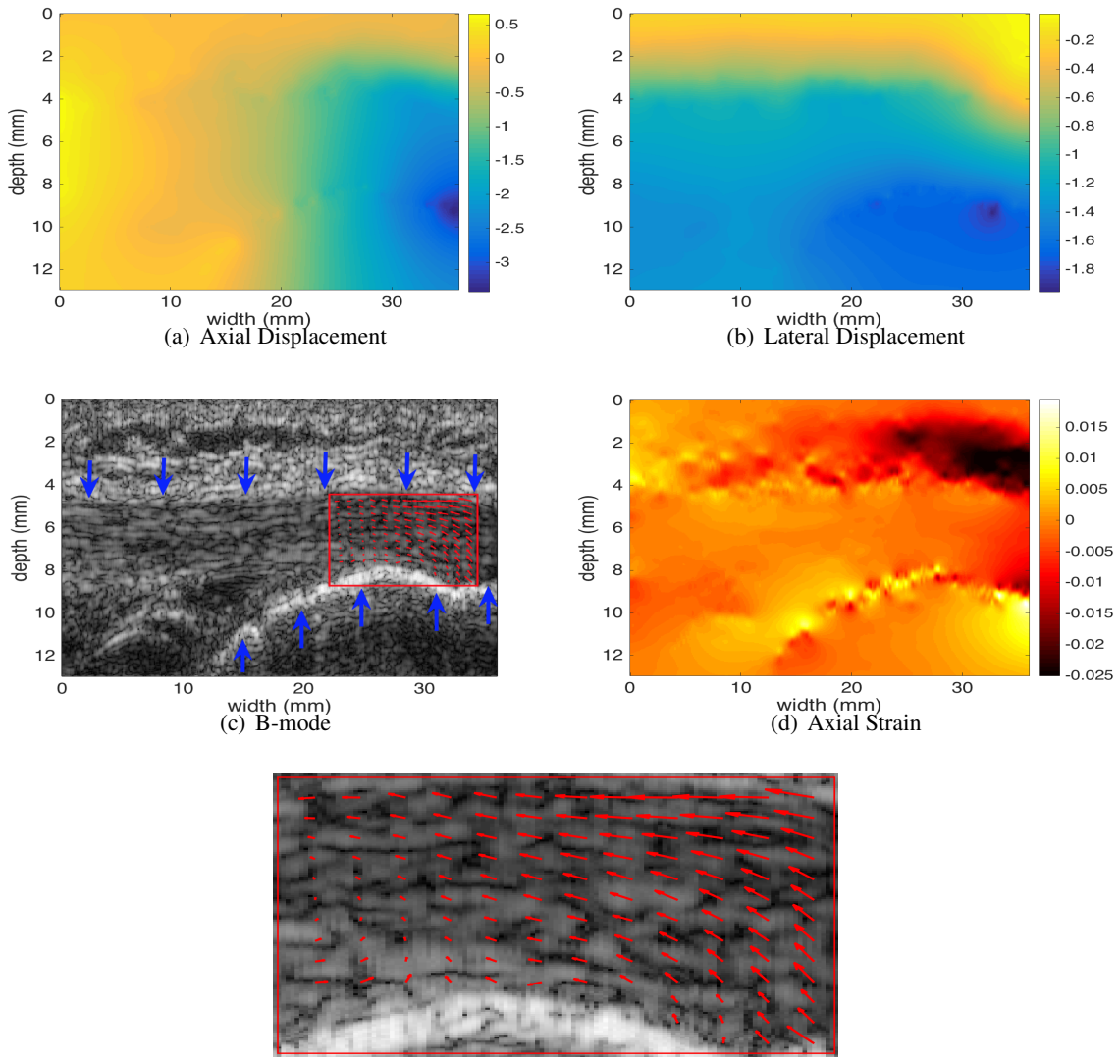

(a) Axial Displacement

(b) Lateral Displacement

(c) B-mode

(d) Axial Strain

(e) Strain directions

Figure 3.3: Distal tendon motion during force flexion experiment. (a) and (b) show axial and lateral displacements. (c) is the B-mode image and red arrows represent the strain directions in the tendon. (d) and (e) depict the axial strain and magnified strain directions respectively.

the subject freely flexed their knee, and ultrasound data was collected from the patellar tendon, and all subjects signed a consent form. Valgus stress and knee flexion generates strain in the MCL and patellar tendon respectively, and we examined whether this strain can be measured using ATME. RF data was collected with an Alpinion ultrasound machine (Bothell, WA) with an L3-12 linear transducer at the centre frequency of 11MHz and sampling frequency of 40MHz. Ligaments and tendons play a significant role in musculoskeletal (MSK) biomechanics, and constantly change due to factors such as aging, injury, disease or exercise. Conventional B-mode ultrasonography has been widely used as a first line diagnostic modality for superficial structures such as the patellar tendon and MCL. Strain imaging captures dynamics of tissue motion and captures deformations of the patellar tendon and MCL, which are not directly available in B-mode images. These deformation patterns reveal mechanical properties of tendon and therefore may reveal important pathology otherwise hidden in the B-mode scans (Chimenti et al., 2016).

Fig. 3.3(a) and (b) show the displacement of the distal tendon (lower portion of patellar tendon connected to tibia) during *in-vivo* forced flexion. The B-mode image is demonstrated in (c). Red arrows represent strain directions and their relative amplitudes in a region of interest. The patellar tendon is marked with blue arrows. The axial strain is shown in (d) wherein we can clearly distinguish the boundaries of tendon from rest of the tissue. The strain arrows in (c) are magnified and depicted in (e) for better visualization. The results in (e) are in good agreement with our expectation of strain in the patellar tendon: the strain is relatively high close to the patella (the hyperechoic dome-shaped structure in bottom left of (c) with the shadow underneath), where it is getting pulled by the joint. The strain is also tensile (arrows pointing to the left) at the top, and compressive at the bottom (arrows pointing to the right) in (e), as we expect from a bent structure (i.e. the patellar tendon).

Fig. 3.4(a) and (b) demonstrate the motion fields of MCL when the pure valgus stress is applied on the knee. (c) and (d) show the B-mode and strain images respectively. MCL is marked with blue arrows in (c). Strain directions which are shown with red arrows in (c) are enlarged in (e). Again, the strain field corresponds well with what we expect: high tension at the top where the extension is maximum in the bent MCL.

Fig. 3.5 shows B-mode images and also the strain fields calculated for the Patellar tendon and

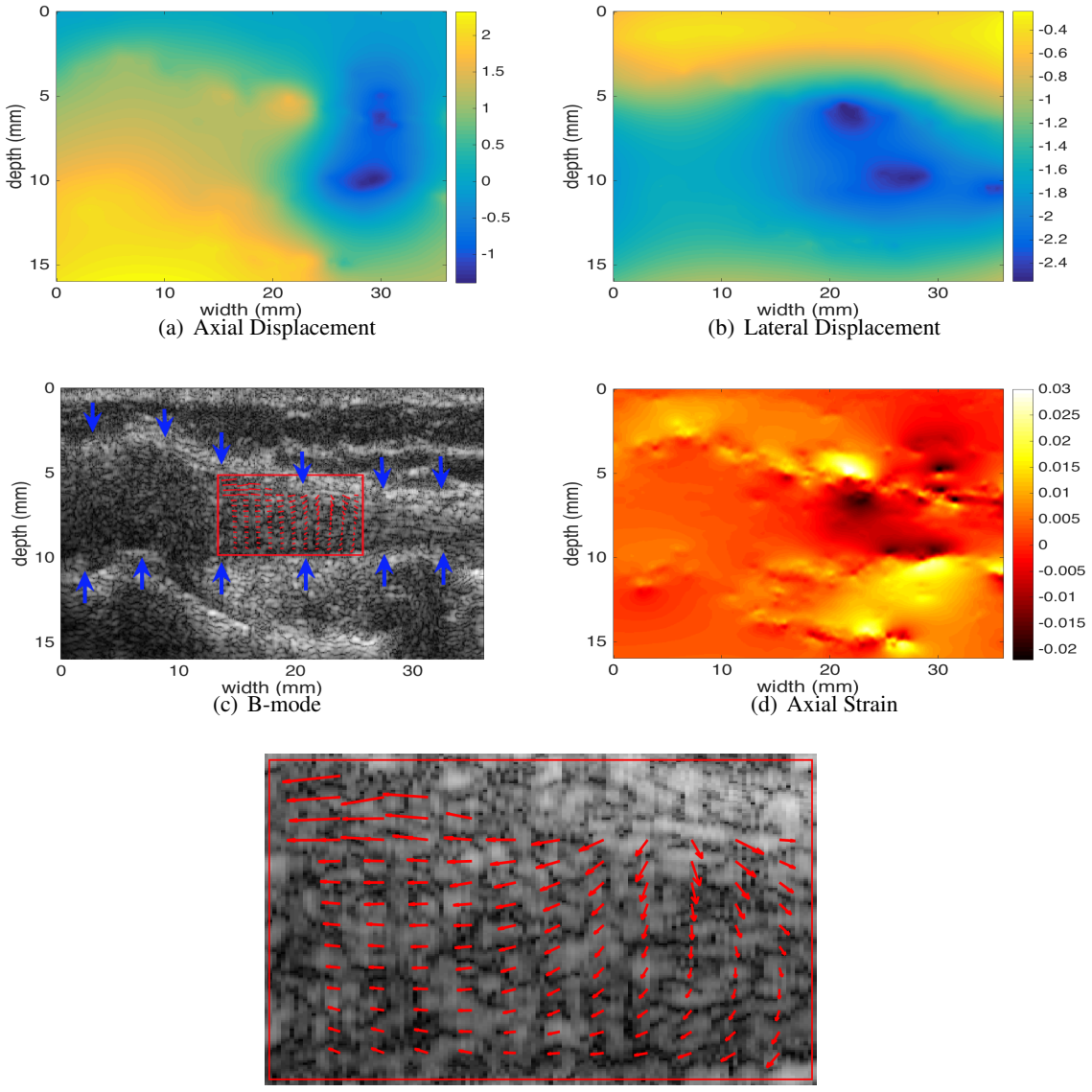

(a) Axial Displacement

(b) Lateral Displacement

(c) B-mode

(d) Axial Strain

(e) Strain directions

Figure 3.4: MCL during pure valgus stress experiment. (a) and (b) show axial and lateral displacements. (c) is the B-mode image and red arrows represent the strain directions in the MCL. (d) and (e) depict the axial strain and magnified strain directions respectively.

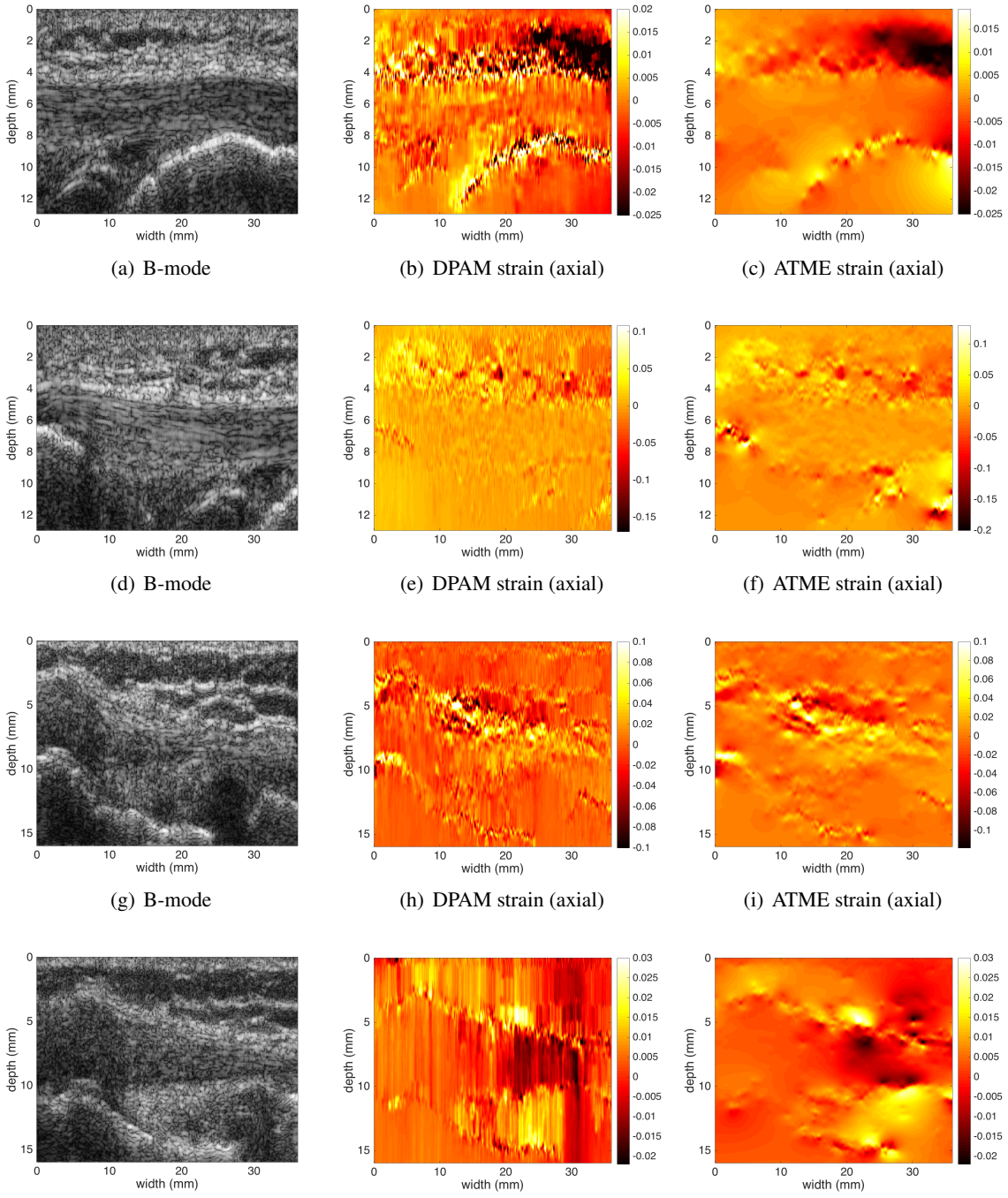

(a) B-mode (b) DPAM strain (axial) (c) ATME strain (axial)

(d) B-mode (e) DPAM strain (axial) (f) ATME strain (axial)

(g) B-mode (h) DPAM strain (axial) (i) ATME strain (axial)

(j) B-mode (k) DPAM strain (axial) (l) ATME strain (axial)

Figure 3.5: comparison between ATME and DPAM methods. (a), (b), and (c) show distal area of patellar tendon during force flexion experiment. (d), (e), and (f) are proximal region of patellar tendon. (g)-(l) are B-mode and strain images of MCL during pure valgus stress experiment.

MCL during flexion. For the purposes of comparison, strain images were also calculated using a previous work, DPAM (Rivaz et al., 2011). In the first row, the distal portion of the knee is shown while the forced flexion is applied to patellar tendon. In the second row, the same experiment is practiced but the proximal portion of the knee is depicted here. Third and forth rows show the MCL when pure valgus stress is placed on the knee. The valgus stress test is performed with the knee at 30° of flexion.

The unitless metrics signal to noise ratio (SNR) and contrast to noise ratio (CNR) are used to quantitatively compare the results (Ophir et al., 1999):

$$\mathrm{CNR} = \frac{C}{N} = \sqrt{\frac{2(\bar{s_b} - \bar{s_t})^2}{\sigma_b^2 + \sigma_t^2}},\ \mathrm{SNR} = \frac{\bar{s}}{\sigma} \tag{19}$$

where $\bar{s_t}$ and $\bar{s_b}$ are the spatial strain average of the target and background, and σ_t^2 and σ_b^2 are the spatial strain variance of the target and background, and $\bar{s}$ and σ are the spatial average and variance of a window in the strain image respectively. The corresponding SNR and CNR values are measured for both DPAM and ATME methods. CNR values are calculated between the target (tendon) and background (outside the target) windows each of size 50 samples $\times$ 50 samples, and are provided in Table 3.1. SNR values are also shown in the table, which are calculated for the background windows. ATME provides substantially higher SNR and CNR values compared to DPAM.

3.4 Conclusion

In this chapter, we introduced a novel technique to calculate both axial and lateral displacement fields between two frames of RF data based on affine transformation prior. Optimization of the main global cost function involves solving a sparse linear system which can be solved in real time and provide the displacement field of the entire image simultaneously. We further applied strain imaging to patellar tendon and MCL, and showed that our proposed technique can be used to predict displacement and strain fields in these tissues. Future work will utilize these dynamical measurements of the patellar tendon and MCL to both improve diagnosis and manage treatment. In the next chapter, we summarize the contributions of this thesis and provide directions for future work.

Chapter 4

Conclusion and Future Work

4.1 Conclusion

Ultrasound elastography has numerous clinical applications in monitoring and treatment of injuries and diseases because pathology usually affects tissue elasticity. It is considered as a non-invasive, convenient, and real-time imaging modality that has been successfully translated from benchside to bedside. In this thesis, we focused on quasi-static elastography wherein tissue deformation is slow and is generated by slowly palpating the tissue with the hand-held ultrasound probe. Numerous techniques have been developed to calculate time-delay estimation between pre- and post-compression images, but ultrasound data is highly noisy and previous work suffers from inaccurate displacement estimates.

In this thesis, we first introduced GLUE, a novel technique for calculating both axial and lateral displacement fields between two frames of RF data. Optimization of the main global cost function involves solving a sparse linear system which can be solved in real time. We estimated the displacement field of the entire image simultaneously, which led to substantial improvement over state of the art. Our implementation of GLUE in MATLAB takes only 0.7 sec on a typical CPU. Therefore, our technique is highly suitable for implementation in commercial ultrasound systems. We have also made an implementation of GLUE available online, which will facilitate knowledge transfer and will amplify the impact of this work.

We further proposed ATME for efficient and robust estimation of the initial displacement field.

We model tissue deformation using a 2D affine transformation to calculate an approximate initial displacement for the GLUE framework. Since 2D affine transformation has only six degrees of freedom (DOF), it can be efficiently estimated by minimizing a quadratic error measure. Axial and lateral displacement fields between two frames of RF data are calculated based on the prior of affine transformation model. Optimization of the main cost function of GLUE with the efficient and robust initial displacement can be solved in real time.

We applied our elastography techniques on finite element simulation data as well as phantom experiments. We further tested our algorithms using challenging real data obtained from human subjects in several different applications of liver tumor, liver ablation, patellar tendon, medial collateral ligament as well as rotator cuff. All of the experiments showed that our method outperforms state of the art elastography techniques.

4.2 Future Work

In this thesis, a regularized cost function formulated that consists of RF data term and prior information of displacement continuity. The axial and lateral displacement maps are achieved through optimization of this nonlinear cost function. Four regularization coefficients in the cost function are tuned manually. Although the elastography parameters can be tuned based on the application in ultrasound machines (as it is often done in preset imaging modes of commercial ultrasound machines), automatic adjustment of these coefficients based on image content can reduce the user-dependency of the proposed techniques.

As described in chapter 2, the first order Taylor expansion is used to make the cost function linear. As a future work, higher order Taylor expansions can be used along with an appropriate optimization technique to improve both accuracy and convergence rate. Furthermore, the GLUE cost function incorporates the displacement continuity between the target sample and its two neighboring samples. It would also be important to investigate displacement continuity for four neighboring samples instead of only two of them. This will enforce more regularization which may improve the results.

Most ultrasound RF frames have spatial bias which makes estimation of tissue displacement

difficult at the boundaries of the image. The spatial bias is not the same at the top and bottom of the ultrasound images and furthermore depends on the acoustic and attenuation properties of the organ. In this work, we ignored image boundaries by a specified margin and limited our computations to the inner parts of the images. As a future work, these areas can be automatically identified using machine learning approaches to limit their impact on the results.

In this thesis, the GLUE and ATME method are tested on liver data, patellar tendon, and MCL data. Future work will utilize these dynamical measurements of the liver, patellar tendon and MCL to both improve diagnosis and manage treatment. Moreover, these techniques can be tested on different RF data from another body organs in the future work. For example, the tissue stiffness can be calculated for cancer diagnosis and monitoring patient response to chemotherapy or radiation therapy.

References

Abu-Zidan, F. M., Hefny, A. F., Corr, P., et al. (2011). Clinical ultrasound physics. *Journal of emergencies, trauma, and shock*, *4*(4), 501.

Alam, S. K., & Ophir, J. (1997). Reduction of signal decorrelation from mechanical compression of tissues by temporal stretching: Applications to elastography. *Ultrasound in medicine & biology*, *23*(1), 95–105.

Alam, S. K., Ophir, J., & Konofagou, E. E. (1998). An adaptive strain estimator for elastography. *IEEE transactions on ultrasonics, ferroelectrics, and frequency control*, *45*(2), 461–472.

Ara, S., Mohsin, F., Alam, F., Rupa, S. A., Lee, S. Y., Hasan, M. K., & Awwal, R. (2013). Phase-based direct average strain estimation for elastography. *IEEE transactions on ultrasonics, ferroelectrics, and frequency control*, *60*(11), 2266–2283.

Babaniyi, O. A., Oberai, A. A., & Barbone, P. E. (2017). Recovering vector displacement estimates in quasistatic elastography using sparse relaxation of the momentum equation. *Inverse Problems in Science and Engineering*, *25*(3), 326–362.

Bamber, J., Cosgrove, D., Dietrich, C., Fromageau, J., Bojunga, J., Calliada, F., ... others (2013). Efsumb guidelines and recommendations on the clinical use of ultrasound elastography. part 1: Basic principles and technology. *Ultraschall in der Medizin-European Journal of Ultrasound*, *34*(02), 169–184.

Bercoff, J., Tanter, M., & Fink, M. (2004). Supersonic shear imaging: a new technique for soft tissue elasticity mapping. *IEEE transactions on ultrasonics, ferroelectrics, and frequency control*, *51*(4), 396–409.

Bergen, J. R., Anandan, P., Hanna, K. J., & Hingorani, R. (1992). Hierarchical model-based motion

estimation. In *European conference on computer vision* (pp. 237–252).

Bilgen, M., & Insana, M. F. (1996). Deformation models and correlation analysis in elastography. *The journal of the acoustical society of America*, *99*(5), 3212–3224.

Brusseau, E., Kybic, J., Déprez, J.-F., & Basset, O. (2008). 2-d locally regularized tissue strain estimation from radio-frequency ultrasound images: Theoretical developments and results on experimental data. *IEEE TMI*, *27*(2), 145–160.

Catheline, S., Wu, F., & Fink, M. (1999). A solution to diffraction biases in sonoelasticity: the acoustic impulse technique. *The Journal of the Acoustical Society of America*, *105*(5), 2941–2950.

Chaturvedi, P., Insana, M. F., & Hall, T. J. (1998). 2-d companding for noise reduction in strain imaging. *IEEE transactions on ultrasonics, ferroelectrics, and frequency control*, *45*(1), 179–191.

Chen, H., Shi, H., & Varghese, T. (2007). Improvement of elastographic displacement estimation using a two-step cross-correlation method. *Ultrasound in medicine & biology*, *33*(1), 48–56.

Chen, X., Zohdy, M. J., Emelianov, S. Y., & O'Donnell, M. (2004). Lateral speckle tracking using synthetic lateral phase. *IEEE transactions on ultrasonics, ferroelectrics, and frequency control*, *51*(5), 540–550.

Chimenti, R. L., Flemister, A. S., Ketz, J., Bucklin, M., Buckley, M. R., & Richards, M. S. (2016). Ultrasound strain mapping of achilles tendon compressive strain patterns during dorsiflexion. *Journal of biomechanics*, *49*(1), 39–44.

Dickinson, R., & Hill, C. (1982). Measurement of soft tissue motion using correlation between a-scans. *Ultrasound in medicine & biology*, *8*(3), 263–271.

Doyley, M. (2012). Model-based elastography: a survey of approaches to the inverse elasticity problem. *Physics in medicine and biology*, *57*(3), R35.

Doyley, M. M., Bamber, J. C., Fuechsel, F., & Bush, N. L. (2001). A freehand elastographic imaging approach for clinical breast imaging: system development and performance evaluation. *Ultrasound in medicine & biology*, *27*(10), 1347–1357.

Ebbini, E. S. (2006). Phase-coupled two-dimensional speckle tracking algorithm. *IEEE transactions on ultrasonics, ferroelectrics, and frequency control*, *53*(5), 972–990.

Friemel, B. H., Bohs, L. N., & Trahey, G. E. (1995). Relative performance of two-dimensional speckle-tracking techniques: normalized correlation, non-normalized correlation and sum-absolute-difference. In *Ultrasonics symposium, 1995. proceedings., 1995 ieee* (Vol. 2, pp. 1481–1484).

Geman, S., Bienenstock, E., & Doursat, R. (1992). Neural networks and the bias/variance dilemma. *Neural computation*, *4*(1), 1–58.

Gennisson, J.-L., Deffieux, T., Fink, M., & Tanter, M. (2013). Ultrasound elastography: principles and techniques. *Diagnostic and interventional imaging*, *94*(5), 487–495.

Goksel, O., Eskandari, H., & Salcudean, S. E. (2013). Mesh adaptation for improving elasticity reconstruction using the fem inverse problem. *IEEE transactions on medical imaging*, *32*(2), 408–418.

Grondin, J., Wan, E., Gambhir, A., Garan, H., & Konofagou, E. E. (2015). Intracardiac myocardial elastography in canines and humans in vivo. *IEEE transactions on ultrasonics, ferroelectrics, and frequency control*, *62*(2), 337–349.

Hall, T. J., Barbone, P., Oberai, A. A., Jiang, J., Dord, J. F., Goenezen, S., & Fisher, T. G. (2011). Recent results in nonlinear strain and modulus imaging. *Current medical imaging reviews*, *7*(4), 313.

Hall, T. J., Zhu, Y., & Spalding, C. S. (2003). In vivo real-time freehand palpation imaging. *Ultrasound in medicine & biology*, *29*(3), 427–435.

Hashemi, H. S., Boily, M., Martineau, P. A., & Rivaz, H. (2017). Ultrasound elastography: Efficient estimation of tissue displacement using an affine transformation model. In *Spie medical imaging* (pp. 1013903–1013903).

Hashemi, H. S., & Rivaz, H. (2017). Global time-delay estimation in ultrasound elastography. In (p. In press). IEEE transactions on ultrasonics, ferroelectrics, and frequency control.

Hiltawsky, K. M., Krüger, M., Starke, C., Heuser, L., Ermert, H., & Jensen, A. (2001). Freehand ultrasound elastography of breast lesions: clinical results. *Ultrasound in medicine & biology*, *27*(11), 1461–1469.

Hoerig, C., Ghaboussi, J., Fatemi, M., & Insana, M. F. (2016). A new approach to ultrasonic elasticity imaging. In *Spie medical imaging* (pp. 97900G–97900G).

Hoogeman, M. S., van Herk, M., de Bois, J., & Lebesque, J. V. (2005). Strategies to reduce the systematic error due to tumor and rectum motion in radiotherapy of prostate cancer. *Radiotherapy and oncology*, *74*(2), 177–185.

Jensen, J. A. (1996). Field: A program for simulating ultrasound systems. In *10th nordic-baltic conference on biomedical imaging, vol. 4, supplement 1, 351–353.*

Jiang, J., & Hall, T. J. (2015). A coupled subsample displacement estimation method for ultrasound-based strain elastography. *Physics in medicine and biology*, *60*(21), 8347.

Khodadadi, H., Aghdam, A. G., & Rivaz, H. (2015). Edge-preserving ultrasonic strain imaging with uniform precision. In *Engineering in medicine and biology society (embc), 2015 37th annual international conference of the ieee* (pp. 3835–3838).

Konofagou, E., & Ophir, J. (1998). A new elastographic method for estimation and imaging of lateral displacements, lateral strains, corrected axial strains and poissons ratios in tissues. *Ultrasound in medicine & biology*, *24*(8), 1183–1199.

Kuzmin, A., Zakrzewski, A. M., Anthony, B. W., & Lempitsky, V. (2015). Multi-frame elastography using a handheld force-controlled ultrasound probe. *IEEE transactions on ultrasonics, ferroelectrics, and frequency control*, *62*(8), 1486–1500.

Lindop, J. E., Treece, G. M., Gee, A. H., & Prager, R. W. (2006). 3d elastography using freehand ultrasound. *Ultrasound in medicine & biology*, *32*(4), 529–545.

Lindop, J. E., Treece, G. M., Gee, A. H., & Prager, R. W. (2008). Phase-based ultrasonic deformation estimation. *Ultrasonics, Ferroelectrics, and Frequency Control, IEEE Transactions on*, *55*(1), 94–111.

Lopata, R. G., Nillesen, M. M., Hansen, H. H., Gerrits, I. H., Thijssen, J. M., & De Korte, C. L. (2009). Performance evaluation of methods for two-dimensional displacement and strain estimation using ultrasound radio frequency data. *Ultrasound in medicine & biology*, *35*(5), 796–812.

Maurice, R. L., & Bertrand, M. (1999). Lagrangian speckle model and tissue-motion estimation-theory [ultrasonography]. *IEEE transactions on medical imaging*, *18*(7), 593–603.

Mousavi, S. R., Sadeghi-Naini, A., Czarnota, G. J., & Samani, A. (2014). Towards clinical prostate ultrasound elastography using full inversion approach. *Medical physics*, *41*(3).

Nahiyan, A., & Hasan, M. K. (2015). Hybrid algorithm for elastography to visualize both solid and fluid-filled lesions. *Ultrasound in medicine & biology*, *41*(4), 1058–1078.

Nightingale, K., Soo, M. S., Nightingale, R., & Trahey, G. (2002). Acoustic radiation force impulse imaging: in vivo demonstration of clinical feasibility. *Ultrasound in medicine & biology*, *28*(2), 227–235.

O'Donnell, M., Skovoroda, A. R., Shapo, B. M., & Emelianov, S. Y. (1994). Internal displacement and strain imaging using ultrasonic speckle tracking. *IEEE transactions on ultrasonics, ferroelectrics, and frequency control*, *41*(3), 314–325.

Ophir, J., Alam, S., Garra, B., Kallel, F., Konofagou, E., Krouskop, T., & Varghese, T. (1999). Elastography: ultrasonic estimation and imaging of the elastic properties of tissues. *Proceedings of the Institution of Mechanical Engineers, Part H: Journal of Engineering in Medicine*, *213*(3), 203–233.

Ophir, J., Cespedes, I., Ponnekanti, H., Yazdi, Y., & Li, X. (1991). Elastography: a quantitative method for imaging the elasticity of biological tissues. *Ultrasonic imaging*, *13*(2), 111–134.

Pan, X., Liu, K., Shao, J., Gao, J., Huang, L., Bai, J., & Luo, J. (2015). Performance comparison of rigid and affine models for motion estimation using ultrasound radio-frequency signals. *IEEE transactions on ultrasonics, ferroelectrics, and frequency control*, *62*(11), 1928–1943.

Parker, K., Doyley, M., & Rubens, D. (2012). Corrigendum: Imaging the elastic properties of tissue: the 20 year perspective. *Physics in medicine & biology*, *57*(16), 5359–5360.

Pellot-Barakat, C., Frouin, F., Insana, M. F., & Herment, A. (2004). Ultrasound elastography based on multiscale estimations of regularized displacement fields. *Medical Imaging, IEEE Transactions on*, *23*(2), 153–163.

Pesavento, A., Perrey, C., Krueger, M., & Ermert, H. (1999). A time-efficient and accurate strain estimation concept for ultrasonic elastography using iterative phase zero estimation. *IEEE transactions on ultrasonics, ferroelectrics, and frequency control*, *46*(5), 1057–1067.

Petitclerc, L., Sebastiani, G., Gilbert, G., Cloutier, G., & Tang, A. (2016). Liver fibrosis: Review of current imaging and mri quantification techniques. *Journal of Magnetic Resonance Imaging*.

Rivaz, H., Boctor, E., Foroughi, P., Zellars, R., Fichtinger, G., & Hager, G. (2008). Ultrasound elastography: a dynamic programming approach. *Medical Imaging, IEEE Transactions on*,

27(10), 1373–1377.

Rivaz, H., Boctor, E. M., Choti, M. A., & Hager, G. D. (2011). Real-time regularized ultrasound elastography. *Medical Imaging, IEEE Transactions on*, *30*(4), 928–945.

Rivaz, H., Boctor, E. M., Choti, M. A., & Hager, G. D. (2014). Ultrasound elastography using multiple images. *Medical image analysis*, *18*(2), 314–329.

Sato, E., Nakayama, K., Nakamura, K., Ishikawa, M., Katagiri, H., & Kyo, S. (2015). A case with life-threatening uterine bleeding due to postmenopausal uterine arteriovenous malformation. *BMC women's health*, *15*(1), 10.

Shao, Y.-H., Zhang, C.-H., Wang, X.-B., & Deng, N.-Y. (2011). Improvements on twin support vector machines. *IEEE transactions on neural networks*, *22*(6), 962–968.

Song, P., Zhao, H., Manduca, A., Urban, M. W., Greenleaf, J. F., & Chen, S. (2012). Comb-push ultrasound shear elastography (cuse): a novel method for two-dimensional shear elasticity imaging of soft tissues. *IEEE transactions on medical imaging*, *31*(9), 1821–1832.

Szeliski, R. (2012). *Bayesian modeling of uncertainty in low-level vision* (Vol. 79). Springer Science & Business Media.

Tang, A., Cloutier, G., Szeverenyi, N. M., & Sirlin, C. B. (2015). Ultrasound elastography and mr elastography for assessing liver fibrosis: Part 1, principles and techniques. *American Journal of Roentgenology*, *205*(1), 22–32.

Tanter, M., Bercoff, J., Athanasiou, A., Deffieux, T., Gennisson, J.-L., Montaldo, G., ... Fink, M. (2008). Quantitative assessment of breast lesion viscoelasticity: initial clinical results using supersonic shear imaging. *Ultrasound in medicine & biology*, *34*(9), 1373–1386.

Tanter, M., & Fink, M. (2014). Ultrafast imaging in biomedical ultrasound. *IEEE transactions on ultrasonics, ferroelectrics, and frequency control*, *61*(1), 102–119.

Thomas, L. H. (1949). Elliptic problems in linear difference equations over a network. *Watson Sci. Comput. Lab. Rept., Columbia University, New York*, *1*.

Treece, G., Lindop, J., Chen, L., Housden, J., Prager, R., & Gee, A. (2011). Real-time quasi-static ultrasound elastography. *Interface focus*, 1-13.

Treece, G. M., Lindop, J. E., Gee, A. H., & Prager, R. W. (2008). Freehand ultrasound elastography with a 3-d probe. *Ultrasound in medicine & biology*, *34*(3), 463–474.

Walker, W. F., & Trahey, G. E. (1995). A fundamental limit on delay estimation using partially correlated speckle signals. *IEEE Transactions on Ultrasonics, Ferroelectrics, and Frequency Control*, *42*(2), 301–308.

Wen, Z., Yin, W., & Zhang, Y. (2012). Solving a low-rank factorization model for matrix completion by a nonlinear successive over-relaxation algorithm. *Mathematical Programming Computation*, *4*(4), 333–361.

Yamakawa, M., Nitta, N., Shiina, T., Matsumura, T., Tamano, S., Mitake, T., & Ueno, E. (2003). High-speed freehand tissue elasticity imaging for breast diagnosis. *Japanese journal of applied physics*, *42*(5S), 3265.

Young, D. M. (1971). *Iterative solution of large linear systems*. Elsevier.

Yuan, L., & Pedersen, P. C. (2015). Analytical phase-tracking-based strain estimation for ultrasound elasticity. *IEEE transactions on ultrasonics, ferroelectrics, and frequency control*, *62*(1), 185–207.

Zahiri, R., & Salcudean, S. (2006, Oct.). Motion estimation in ultrasound images using time domain cross correlation with prior estimates. *IEEE Trans. Biomed. Eng.*, *53*(10), 1990-2000.